SYNTHESIS OF SILICA NANOFIBERS EMBEDDED WITH GOLD NANOPARTICLES BY LASER PULSES AND SPUTTERING TECHNIQUES

by

Sarah Hamza

B.Sc.Eng, University of New Brunswick, 2015

A THESIS SUBMITTED IN PARTIAL FULFILLMENT OF THE REQUIREMENTS FOR THE DEGREE OF

Masters of Science in Engineering

In the Graduate Academic Unit of Mechanical Engineering

Supervisor:	Amirkianoosh Kiani, PhD, Mechanical Engineering
Examining Board:	Rickey Dubay, PhD, Mechanical Engineering
	Mohsen Mohammadi, PhD, Mechanical Engineering
	Andy Simoneau, PhD, Mechanical Engineering (Chair)
	Anna Ignaszak, PhD, Chemistry (External)

This thesis is accepted by the Dean of Graduate Studies

THE UNIVERSITY OF NEW BRUNSWICK

May, 2017

© Sarah Hamza, 2017

Abstract

Many biomedical sensing applications require high electrical sensitivity as well as a method to control and implement them into biological applications. This requires a material to have both conductive and biocompatible properties. The lack of functional stability for implanted sensors has caused their restriction to short-term usage. Increasing the biocompatibility of these sensing devices generally causes a reduction in the overall conductivity due to the oxidation of the substrate. Silicon is becoming a more feasible and available option for use in these applications due to its semiconductor properties and availability. Previous work has proven the biocompatibility of porous Silicon through in-vitro testing with both SBF and NIH 3T3 culturing. A method to fabricate fibrous Silicon structures as well as control the conductivity of the latter through laser processing techniques and two coating methods are outlined in this thesis. The first involved Gold embedding through sputtering techniques, while the other utilized pre-coated Silicon <Au1000> achieved through PVD. An Nd:YAG pulsed nanosecond laser was employed to process the single crystalline Silicon wafers at a variety of line spacings, overlaps, and average powers. Controlling the scanning parameters were seen to induce the formation of nanofibrous structures. The conductivity of the samples were found to be dependent on both quantum effects and the overall Gold concentration on the surface. A biocompatibility assessment has shown traces of the elements necessary for the formation of hydroxyapatite. Overall, the method outlined in this research offers an economical and effective way to process Silicon into porous and fibrous structures while enhancing the conductivity and biocompatibility for the advancement of potential biomedical sensing and conductive tissue engineering applications.

Dedication

This thesis is dedicated to my parents who have supported me in every possible way and have given me all the opportunities to succeed. I'm sorry this isn't the PhD you hoped for.

Acknowledgements

I would first and foremost like to thank my supervisor, who's hard work and dedication to his field and this project have not only taught me great value and allowed me to succeed, but he has also been an invaluable source of inspiration and motivation towards my future.

I would like to further acknowledge and thank all those involved in the development and completion of this project including the staff of Mechanical Engineering and the Microscopy lab at UNB. A special thank you to my committee members for taking the time to attend, assess, and provide me with their valuable feedback as well.

I would also like to express my gratitude to my colleagues Candace Colpitts and Babak Nagshine for their continued support and assistance throughout my degree. To my family and friends, thank you all for your continued trust, support, and encouragement. I am blessed to have you all in my life.

Table of Contents

Abstract ii
Dedication iii
Acknowledgements iv
List of Figures vii
List of Tables viii
Nomenclature ix
List of Acronyms xi
1.0 Introduction 1
1.1 Biomaterials 1
1.2 Biocompatible Sensors 6
1.3 Sensor Materials for Biological Applications 7
1.4 Surface Modification of Silicon 9
1.4.1 Chemical Etching 9
1.4.2 Photolithography 9
1.4.3 Laser Processing 9
1.4.4 Thin Film Deposition Methods 14
1.5 Silicon 17
1.6 Osseointegration 19
1.7 Research Objectives 20
2.0 Physical Modelling 22
2.1 Temperature 22
2.2 Evaporation Rate 26
2.3 Plasma Pressure 28
2.4 Electrical Conductivity 30
3.0 Experimental Setup and Procedure 33
3.1 Laser Processing 34
3.2 Microscopy and Surface Characterization 35
3.3 Light Spectroscopy 37
3.4 Impedance Spectroscopy 37
3.5 Image Analysis 38
3.6 Biocompatibility 38

3.7 Statistical Analysis 39
4.0 Generation of Nanofibrous Structures 40
4.1 Line Spacing Effects 41
4.2 Overlap Effects 42
4.3 Light Absorption 44
5.0 Synthesis of Silica Nanofiber/Gold Nanoparticles Composite Induced by Laser Pulses 52
5.1 Roughness 56
5.1 Conductivity 57
5.2 Biocompatibility 61
6.0 Silica/Gold Hybrid Nanofibers Induced by Laser Processing of Silicon Coated by Gold Thin-Film 63
6.1 Roughness 74
6.2 Conductivity 75
6.2 Biocompatibility 79
7.0 Summary and Future Work 81
7.1 Summary 81
7.2 Future Research 83
Appendices 90
Curriculum Vitae .....

List of Figures

Fig. 1 Depiction of the formation of nanofibers on the surface of Silicon by pulsed laser deposition.....12
Fig. 2 Depiction of the heated regions and the difference in pulse duration between the nanosecond and femtosecond.....13
Fig. 3 Approach I: Gold sputtering of laser generated Silicon dioxide nanofibers. 33
Fig. 4 Approach II: Laser processing of Au-coated (1000 nm) Si wafers.....34
Fig. 5 Experimental setup of the Nd:YAG laser system.....35
Fig. 6 Raman spectra of laser processed Silicon; a-Si: amorphous Silicon; c-Si: crystalline Silicon.....41
Fig. 7 SEM images of laser processed Silicon at five overlaps: (A) 0.15 mm, (B) 0.1 mm, (C) 0.025mm. ...42
Fig. 8 SEM images of laser processed Silicon at 0.025 mm line spacing. (A) 1 OL, (B) 3 OL, (C) 5 OL.....43
Fig. 9 Roughness measurements of Silicon samples processed at 12 W, 0.025 mm line spacing, and overlaps ranging from one to five. 44
Fig. 10 Light absorption of laser treated Silicon samples at 1 and 3 OL and at line spacings of 0.025 mm, 0.10 mm, and 0.15 mm. 45
Fig. 11 Light absorption of laser treated Silicon samples at 1 OL and line spacings of 0.025 mm, 0.10 mm, and 0.15 mm.....46
Fig. 12 Theoretical average temperatures reached by laser-ablated single crystalline Silicon samples.....48
Fig. 13 Theoretical (A) number of evaporated atoms by successive pulses and (B) evaporation rate for single pulse ablation at varying absorption coefficients. 50
Fig. 14 Plasma pressure and interface thickness estimated at different average powers. 51
Fig. 15 TEM and EDX images of laser processed Silicon at 0.025mm. (A) 1 OL, (B) 3 OL, (C) 5 OL, (D) 5 OL.....53
Fig. 16 Average fiber diameters calculated from SEM images at 1 OL, 3 OL, and 5OL.....53
Fig. 17 Average Silicon particle diameters of samples Gold sputtered for 8 minutes. (A) 1 OL 0.025 mm, (B) 5 OL 0.025 mm, (C) 5 OL 0.15 mm.....54
Fig. 18 Average Gold particle diameters of samples Gold sputtered for 8 minutes. (A) 1 OL 0.025mm, (B) 5 OL 0.025mm, (C) 5 OL 0.15mm.....55
Fig. 19 Gold concentrations found on laser processed Silicon sputtered with Gold for 8 minutes at 1 OL 0.025mm, 5 OL 0.025mm, and 5 OL 0.15mm.....56
Fig. 20 Roughness measurements of samples tested at one and five overlaps at different sputtering times (0, 4, or 8 minutes).....57
Fig. 21 Conductivity of Gold sputtered Silicon samples. (A) 1 OL, (B) 2 OL, (C) 8 minutes of Gold sputtering at 1 and 2 OL.....58
Fig. 22 Conductivity of processed Silicon samples at one, two, and three overlaps.....59
Fig. 23 Conductivity of Gold sputtered Silicon samples at one overlap with a sputtering duration of zero, four, or eight minutes. 60
Fig. 24 Conductivity of processed Silicon samples at two and three overlaps with either no Gold or Gold sputtered for eight minutes.....60
Fig. 25 Experimental interparticle distances of Gold sputtered Silicon samples. (A) 1 OL, (B) 5 OL. 61
Fig. 26 EDX results of untreated and laser treated samples.....62
Fig. 27 TEM images of laser processed evaporated Gold Silicon wafer at 0.025mm line spacing and at different overlaps and average power: (A) 1 OL 2.35 W, (B)1 OL 4 W, (C) 1 OL 9 W, (D) 5 OL 2.35 W, (E) 5 OL 4 W, (F)5 OL 9 W.....64
Fig. 28 Average Silicon and Gold particle diameters for thin film samples. 65
Fig. 29 EDX results comparing samples at 9 W processed at one and five overlaps.....65
Fig. 30 Gold concentrations found on laser processed Gold coated at 0.025 mm line spacing and 1 OL and 5OL.....66
Fig. 31 FESEM images of processed Gold coated Silicon at 2.35 W and 0.025mm line spacing. (A) 1 OL, (B) 3 OL, (C) 5 OL. 67
Fig. 32 EDX results for sample treated at 2.35 W showing traces of Oxygen, Silicon, and Gold. 67
Fig. 33 Processed Gold coated Silicon at 4W and 0.01 mm line spacing. SEM images: (A) 1 OL, (B) 3 OL, (C) 5 OL. FESEM backscattering images: (D) 1 OL, (E) 3 OL, (F) 5 OL. 68
Fig. 34 Processed Gold coated Silicon at 4W and 0.025 mm line spacing. SEM images: (A) 1 OL, (B) 3 OL, (C) 5 OL. FESEM backscattering images: (D) 1 OL, (E) 3 OL, (F) 5 OL. 69

Fig. 35. Processed Gold coated Silicon at 9W and 0.05 mm line spacing. SEM images: (A) 1 OL, (B) 3 OL, (C) 5 OL. FESEM backscattering images: (D) 1 OL, (E) 3 OL, (F) 5 OL. 70
Fig. 36 FESEM images of processed Gold coated Silicon at 9W and 0.025 mm line spacing. (A) 1 OL, (B) 3 OL, (C) 5 OL. 71
Fig. 37 FESEM images of processed Gold coated Silicon at a line spacing of 0.025 mm and one overlap. FESEM images: (A) 4 W, (B) 9 W. FESEM backscattering images: (C) 4 W, (D) 9 W. 72
Fig. 38 SEM images of processed Gold coated Silicon at 12 W. (A) 0.025 mm, 1 OL, (B) 0.025 mm, 3 OL, (C) 0.025 mm, 5 OL, (D) 0.01 mm, 1 OL, (E) 0.01 mm, 3 OL, (F) 0.01 mm, 5 OL. 73
Fig. 39 Plotted EDX results of thin film samples processed at 0.025mm and 4 W. 74
Fig. 40 Roughness values for Gold coated samples at one and five overlaps and different powers. 75
Fig. 41 Conductivity of thin film processed samples at (A) 2.35W at 1 and 5 OL, (B) 4W and 9W at 1 and 5 OL. 76
Fig. 42 Conductivity of thin film processed samples at (A) 2.35W at 1 and 5 OL, (B) 4W and 9W at 1 and 5 OL. 77
Fig. 43 Conductivity of thin film processed samples at 2.35 W and 4 W. (A) 1 OL, (B) 5 OL. 78
Fig. 44 Conductivity of thin film processed samples at 1 OL and 5 OL. (A) 2.35 W, (B) 4 W. 79
Fig. 45 EDX results of untreated and laser treated sample. 80

List of Tables

Table 1: Ingredient list for preparation of SBF [65]. 38
Table 2: Properties of Silicon at Room Temperature [73] 91
Table 3: Properties of Gold at Room Temperature [74] 92

Nomenclature

A_{foc}	**Laser Irradiation Focal Spot Area (m)**
α	**Absorption Coefficient**
c_p	**Specific Heat (J/kg K)**
D_t	**Laser Pulse Dwell Time (s)**
d	**Diameter (m)**
f	**Frequency (Hz)**
h	**Planck's Constant (Js)**
I	**Intensity (W/m^2)**
K	**Residual Energy Coefficient**
k	**Thermal Diffusion Coefficient (m^2/s)**
k_B	**Boltzmann Constant (J/K)**
k_o	**Thermal Conduction Coefficient (W/m K)**
T	**Temperature ($°K$)**
t	**Time (s)**
t_{eq}	**Equilibration Time (s)**
t_p	**Pulse Duration (s)**
t_{pp}	**Pulse Interval (s)**
M_a	**Atomic Mass (kg)**
N_{eff}	**Effective Number of Pulses**
n_{air}	**Density of Air (kg/m^3)**
n_c	**Number of Conductive Particles**

n_i	**Number of Insulating Particles**
L	**Interface Thickness (μm)**
l	**Interparticle Distance (nm)**
m	**Mass of Charge Carriers (kg)**
P	**Power (W)**
$P_{pressure}$	**Plasma Pressure (kbar)**
ρ	**Density (kg/m^3)**
Q	**Heat Energy Generated per Unit Time (W)**
$\emptyset$	**Heat Flux (W/m^2)**
σ_c	**Conductivity of Conductive Substrate (Siemens/cm)**
σ_i	**Conductivity of Insulating Substrate (Siemens/cm)**
R	**Reflection Coefficient**
R_{rep}	**Laser Repetition Rate (Hz)**
R_c	**Radius of Conductive Particles (nm)**
R_i	**Radius of Insulating Particles (nm)**
V	**Volume Fraction**
$V(t)$	**Temperature modified barrier height (eV)**
z	**Depth (m)**
Z	**Mass Burning Rate ($kg/m^2\ s$)**

List of Acronyms

EDX – Energy Dispersive X-ray

FEM – Field Emission Spectroscopy

FESEM – Field Emission Scanning Electron Microscope

SBF – Simulated Body Fluid

SEM – Scanning Electron Microscope

Chapter 1

1.0 Introduction

The challenge to date has been the relay of electrical signals and information to the biological system. A material can be biocompatible in the body however, it may be a very poor conductor and unable to interface the information necessary to the nervous system. The lack of functional stability and biocompatibility of implanted sensors has caused their restriction to short-term usage within biological mediums [1]. Many important applications in the field of biocompatible-sensing also rely on the ability of semiconductors to convert a signal into an electrical response. These sensors are applied in key roles in many individuals' lives from diabetics to patients being screened for diseases. Furthering the research to improve the sensory and biocompatibility of these materials will lead to improvements in the longevity, sensitivity, and efficiency of these applications, whether for internal or external usage.

1.1 Biomaterials

The use and development of biomaterials dates to the early stages of humankind. Due to the proliferation of disease and injuries, humans have attempted to repair and augment the body. Early attempts included the use of wood and bone due to their availability, but with technological advances, these materials were soon replaced by ceramics, polymers and metal alloys. Both performance and functionality were vastly improved with these advancements. It was quickly found that a major concern in the efficacy of the biomaterial

was in its bio-inertness and its ability not to interact with the host organism. For this reason, early stages of development focused on the primary use of inert materials that would prevent rejection in the body. It wasn't until the surfacing of molecular biology in the 1970's that bioactive materials began appearing. Materials that could induce a favorable response in the body became an interesting field of study both in the industry and academia [2].

Implants with biocompatible materials serve the main purpose of reinforcing or replacing defective or damaged tissue. Improving the quality of life of the patient is the main goal, however the short life-span of these implants make them a less preferred alternative. Although having a high-success rate, hip replacements for example have an approximate life span of only 10 – 15 years and require complex and costly surgeries [3, 4]. Advancements in the field of biomaterials has reduced failure rates due to wear or fracture, but there are still many cases of malfunctions arising from the loosening of the implant from its supporting hard tissue. This generally results in increased wear and pain to the patient. The wear can also loosen and increase the amount of debris between the implant and tissue interface causing a macrophage-induced inflammatory response leading to bone loss. For this reason, a high focus and importance has been placed on the development of biomaterials that resist loosening, rapidly integrate with the surrounding tissue, and reduce the patients' recovery period [3].

Biomaterials can be classified into three main categories, they can be bioinert, bioactive, or bioresorbable [5]. The first category, or what is sometimes referred to as the first generation of biomaterials, are those materials that would fulfill their only requirement of reducing the immune response and foreign body attachment by being inert. They are

required to have an appropriate combination of physical, chemical, and mechanical properties to ensure minimal toxicity and reaction from the host organism. The second generation of biomaterials began surging between the years of 1980 to 2000 [5]. Bioactive materials are able to interact with the surrounding biological environment causing a specific response. They may enhance tissue and surface bonding to increase the overall biological response. Not only that, but many bioactive materials were further designed to be replaced by new tissue and progressively degrade. Although many bioactive materials tend to be ceramics and composites, surface modification methods have been shown to induce bioactivity. Since metallic materials are not bioactive, surface modification or the addition of adsorbed proteins or other biomolecules can induce desired cellular responses. Finally, the third generation of biomaterials combines both bioactivity and biodegradability. This results in a material able to induce molecular level changes. Effects at these levels lead to the stimulation of specific and desirable cellular responses depending on the required application. These materials are generally porous and are resorbed into the environment after stimulating a specific cellular response. These are most commonly seen in tissue engineering as a solution to transplantation. The materials chosen for these particular applications have a three-dimensional porous structure able to be resorbed at the same rate as the surrounding tissue is repaired. They also contain a highly porous network made of a combination of micro and macro pores enabling tissue ingrowth, vascularization, and nutrient delivery [5].

The application of biomaterials into the human body is highly dependent on the wounds' healing ability, therefore implants capable of load bearing become difficult due to the availability and limitations of naturally biocompatible materials. Not only is the

biocompatibility of the material of importance, but other important factors including its corrosion resistance, and ability to sustain long-term loading in the human body's harsh environment will help reduce any corrosion and fatigue [3, 6]. Due to their load bearing abilities, certain metals are often considered for these applications. Unlike other materials, electrons in metals interact through metallic interatomic bonding. The non-directional interatomic bonds allow for easier movement of electrons within the lattices compared to ionic or covalently bonded materials. This property allows for their ease in plastic deformation and increased electrical and thermal conductivities [7]. In addition, they are easily processed, have good surface finishes, and can be sterilized using common procedures [8]. In the past, low success rates along with technological advancements led to the replacement of many of these. Today, common metals used in biomedical applications include stainless steels, Cobalt and Titanium alloys.

Stainless steel is a metal which can be processed to match varying grain sizes and alloyed to gain different properties. This metallic material along with Cobalt-Chrome alloys, were some of the first to be successfully incorporated in orthopaedic applications. Compared to others, stainless steel has a lower cost, higher availability, and is easily processed. Due to its elevated Chromium content, the formation of an oxide layer on the surface is encouraged and its resistance to corrosion can be increased. The main drawback to these alloys is that they are commonly stabilized with Nickel or Molybdenum in order to remain austenitic at room temperature, and Nickel has proven to be the cause of unsolved allergenic and toxic effects within the body [5]. Although used for decades, stainless steel has a high susceptibility to crevice corrosion. It is also highly dependent on its design for its application, as extensive deformation highly increases the local strains of the metal. If these

are not kept within the safe limits, fractures may ensue [7]. Other metals such as Cobalt-Chromium based and Titanium alloys exhibit more attractive mechanical and corrosion resistance properties, hence minimizing the use of stainless steel in orthopaedics [5].

Cobalt alloys tend to have lower mechanical properties when cast, however increasing its carbon content resulted in improvements to the wear resistance at the cost of its ease of formability. Cobalt alloys are often enriched with Molybdenum to impart further strength to the metal [7]. Similarly, to stainless steel, these alloys generally contain Nickel, which causes the formation of a corrosive byproduct leading to an undesirable response from the body [8].

Titanium has shown success in the past as a significant biocompatible material [9]. It has shown excellent in vivo corrosion resistance due to its rapid formation of an oxide layer [7]. Its properties tend to include the following: low electrical conductivity, high corrosion resistance, low tendency to form ions in aqueous solutions, superior fracture toughness, fatigue resistance, and a Young's modulus nearing that of bone [3, 10]. With these bulk properties, the main focus has been turned towards surface engineering as most cells and tissues tend to interact solely with the outermost layer of the implant [3]. Previous research experiments have found that oxidizing Titanium resulted in excellent biocompatibility [11]. Unfortunately, toxicity has been shown in some of the Titanium alloys, especially in the more attractive Ti-6Al-4V. It is now no longer considered as a permanent or long-term implant due to its toxic effects causing both nuclear and DNA damage to surrounding cells [12]. Although Titanium has been a desirable biomaterial, its alloys tend to behave poorly in environments prone to friction. The wear causes small particles of Titanium to dissipate into the surrounding tissues [13].

1.2 Biocompatible Sensors

Another important application of biomaterials is in the development of sensors able to interact with the body, whether in-vivo or in-vitro. Their purpose is to convert a biological response into an electrical signal. Most biomedical sensing applications require controllable electrical sensitivity as well as biocompatibility properties. Conductive biomaterials for example can mimic cellular properties through their response to electrical stimuli, making them important in the role of tissue engineering [14]. The interaction of the biomaterial and living tissue can also be regulated by certain properties of the biomaterial, such as its surface topography and wettability [15]. In many biological sensing applications, the low signal-to-noise ratio affects the overall quality of the electrical outputs [16]. Sensor probes and transducers are the most commonly used. The transducer serves the purpose of converting variations in a physical quantity into an electrical signal, which is coupled to a biological element acting as the receptor. The two elements can be coupled through covalent bonding, matrix and membrane entrapment, or physical adsorption. Common biological recognition elements acting as sensors include enzymes, antibodies, receptors and whole cells. They can be used to measure various gases, ions, bacteria and other organic compounds [17].

There are various coupling methods between the substrate and the biological environment in which the sensor is being used. The coupling can be calorimetric, where the heat absorbed or released is measured [18]. It could be potentiometric and the changes in the distribution of charges is measured and results in an electrical potential. It could also be amperometric and be sensitive to redox reactions resulting in electron movement. It can operate optically and respond to light absorbance or reflection between the products and

reactants [17], and finally it may work through piezo-electrics and sense the changes in reactants and products due to their mass [17, 18].

Overall, biocompatible sensing applications can generally and simplistically be broken down into four main components: the sample, the bio-recognition element, the transducer, and signal interpretation. Ideally, these sensors should be appropriately sized to their medium, manufactured at low cost, and self-calibrating to require minimal human interference [17].

1.3 Sensor Materials for Biological Applications

The process of creating surface features leads to changes in the chemical composition, and since many of these materials are alloyed, it is very common for adverse tissue reactions to occur, and an overabundance of cytotoxic elements to pool to the surface [18, 19]. This places a high importance on the consideration of the composition of the implants. As a bulk material, pure Titanium has shown some promising applications, even though its ideal properties are not as desirable without alloys. Titanium is also an expensive material and its conductive properties are lacking compared to others.

Biocompatible sensing materials tend to be costly to produce as well as having a low signal-to-noise ratio. Nanomaterials were introduced as an attempt to reduce the muffling caused by the noise. Two main methods are used to reduce muffling, namely nanotube formation and nanomaterials [16]. Carbon nanotubes are an attractive solution and are generally made of graphene and can be single- or multi-walled [20]. The tubes consist of both metallic and semi-conductive elements and facilitate the transport of electrons from the redox reactions occurring in electroactive species [16, 21]. The success of nanotubes as sensors may be attributed to their increased effective surface area, which decreases the electrode

impedance and increases current [16, 18]. The increased surface area also immobilizes more enzymes thereon in biomedical applications [20]. The atoms at the end of the tubes are highly Oxygenated, which increases electron transfer [16]. However, there are some disadvantages to fabricating carbon nanotubes. For instance, it is an expensive process with a low purity rate, a shortage in alignment control, a lack of aqueous solubility, and high reactivity caused by dangling nanotubes [22].

Porous Silicon, which is formed of a unique structure of nanocrystallites and pores, exhibits properties that are valuable for its use as a biomaterial and biosensor [23]. Its use in biosensing applications has proved to be a much more affordable and viable alternative. Not only is it the second most abundant element after Oxygen, but it also plays a role in bone biology, having shown to quicken the healing process and improve overall bone health [24]. Silicon is versatile in contemporary microprocessing techniques because of its availability and low cost [25, 26]. Silicon-based semiconductors have been the basis of several biosensing applications in vitro, however its biocompatibility had prevented its use in vivo. Silicon's structure controls its physical properties. When Silicon bonds with hydrogen, it forms a highly reactive compound that can form alkyl or hydroxide bonds. By modifying its surface chemistry, the surface of Silicon can be made either hydrophilic or hydrophobic. Silicon can be processed to form macro, micro, and nanopores. The ideal pore diameter for biosensing devices is between 2 and 50 nm. These pore sizes enable biomolecular diffusion and larger surface exposure, resulting in increased biomolecule immobilization compared to 2D surfaces [23]. Silicon's surface-to-volume ratio, surface reactivity, and luminescent properties at the nanoscale make it an excellent material for biosensing applications [25].

1.4 Surface Modification of Silicon

1.4.1 Chemical Etching

Various methods can be used to modify the surface of Silicon substrates. Many of these approaches generate porous structures through chemical methods such as electrochemical etching, requiring specialized equipment and harsh chemicals that render the process sometimes difficult to control [27]. The procedure initially requires thorough cleansing of the wafer. Certain chemicals may highly react to defects in the structure of Silicon and release toxic gases [25, 28]. Electrochemical etching also strongly influences the surface topography making it more difficult to control [29]. Achieving a uniform porous surface using this technique is complex and highly dependent on and sensitive to the etching parameters, also resulting in the production of large quantities of waste [27]. Moreover, a high concentration of hydrogen bonds subside on the surface post preparation, making it highly unstable [25].

1.4.2 Photolithography

Photolithography is another method for modifying the surface of Silicon substrates. This method enables the patterning and control of cell behavior [30]. Its main disadvantage is that due to the optical diffraction of the light beam, the resolution is limited to a maximum of 1 μ in practice. As a result, photolithography is only practical for creating patterns about the size of a cell [29]. Photomask fabrication is also an expensive, lengthy, and a time consuming process [30].

1.4.3 Laser Processing

Laser processing is another technique used to modify the surface of Silicon. It can optimize a material's performance such as its absorption, susceptibility to wear, surface chemistry,

and crystal structure [3]. The field of biomaterials emphasizes on the formation of nanofibrous structures and porous features. These can be produced through laser ablation; whereby high energy can be focused precisely on a single region in a very short time-scale. Surface properties can be controlled in this manner without affecting the bulk of the material [25, 31]. As opposed to conventional chemical methods, laser processing is much faster, allowing for rapid prototyping and mass production applications [32]. This method is ideal not only due to its rapid processing speed, but the parameters of the laser and the material properties can also be designed and optimized to provide the desired functionality. Laser processing is a much better alternative to mechanical, chemical, or electrical texturing methods in terms of its higher precision and larger degrees of control [3].

The removal of material is the result of the energy input from the laser being absorbed and causing the solid's binding energy to be broken. In the classical model, thermodynamic equilibrium is kept meaning that the entirety of the energy ΔE is absorbed and transferred into internal energy ΔU, and hence into a temperature rise ΔT with respect to the heat capacity c_p and the mass of the target m [33]:

$$\Delta E = \Delta U = mc_p \Delta T \qquad \textbf{Eq. 1}$$

This classical process leads to phase transitions, where at a microscopic scale the increase in atomic kinetic energy causes the temperature increase. Unlike other heating methods, the incident light affects primarily the electrons of the material due to its short time scale [33]. Removing material from a solid surface using pulsed laser technology can induce nanoparticle formation. When the laser is shined on a surface, it induces vaporization and removes atoms from the bulk surface, thus enabling the laser pulse to go further into the material. Laser depth depends on factors such as its wavelength and the material's physical

properties. The laser's electromagnetic fields eject electrons by discharging energy and momentum on the surface of the material. The energy transfer involved in the laser's interaction with the material causes its temperature to rise, which in turn causes the formation of an ionized gas known as a plasma that will expand like a shockwave around the laser's focus. Particles are removed from the surface when the laser's intensity (fluence) is greater than the material's ablation threshold. The contents of the plasma take the shape of a plume: a region containing a mixture of ions, electrons, and nanoparticles that are highly reactive as seen in Figure 1 below. When laser ablation is conducted in air, oxidation of the ejected particles may result. As the plume expands, its extremities are cooler than its core [34]. As a result, newly formed particles move toward cooler regions, which causes them to supersaturate, further nucleate, and crystallize into a solid structure. Collisions between gas atoms and the ablated plume in the thin interface layer generate nanoparticles and aggregates. The ambient gas coalesces with the evaporated atoms and ions at high temperatures. As the plume cools, aggregate formation begins. By the end of the laser pulse, aggregate-aggregate and atom-aggregate attachments occur [35]. At ideal plume pressures and temperatures, the particles ejected from the surface may be small enough to reorganize into nanofibrous structures as opposed to micro or macro particle agglomerates as depicted in Fig. 1 [34].

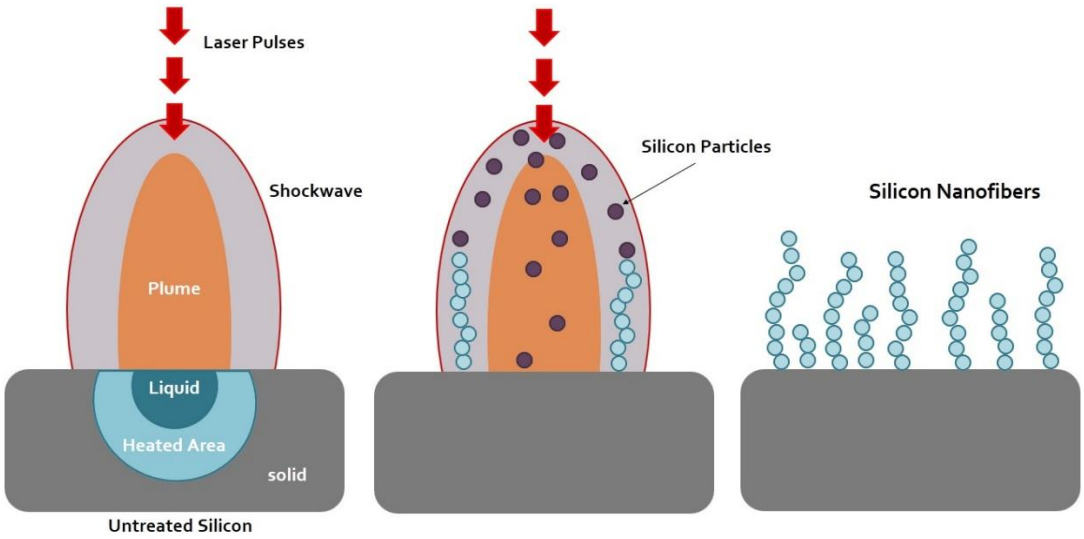

Fig. 1 Depiction of the formation of nanofibers on the surface of Silicon by pulsed laser deposition.

One of the highly dependent parameters on the formation of these fibrous structures on the surface of Silicon is the laser pulse time. Ultra-short lasers have been developed to decrease the interaction time between the substrate and the laser [32]. Rapid pulse times in the femtosecond range have been successful in the formation of nanofibrous structures on the surface of Silicon [36]. These are formed by the rapid cooling of the ejected molten droplets caused by the recoil pressure of the expanding plasma plume [37]. A femtosecond pulse duration does not allow enough time for the electrons to transfer and excite their surroundings, and are instead directly ionized. This results in a much smaller heat affected zone within the sample with no melting. Ultra-short laser pulses with durations below 150 fs do not undergo target modifications until after the laser pulse, hence not affecting absorption properties of the material. This makes it much more attractive for cutting applications where a clean cut is required as the laser does not interact with the ablated material and hence sputter the target surface. These however come at a high price, making them less accessible in many industries. Less expensive alternatives include pulses lasting

at the nanosecond scale, which are much more widely available in manufacturing sectors. Nanosecond pulse durations have a much deeper and larger heated region as seen in Fig. 2. It takes an electron approximately one femtosecond to move from one atom to the other, giving it enough time to transfer and excite the surrounding material before ejection. As the plume expands, the laser pulse has yet to end, thus causing the coupling of the laser energy into the emission of atoms and ions forming the plasma. The bond breaking causes the material to respond through surface relaxation and reorganization [33].

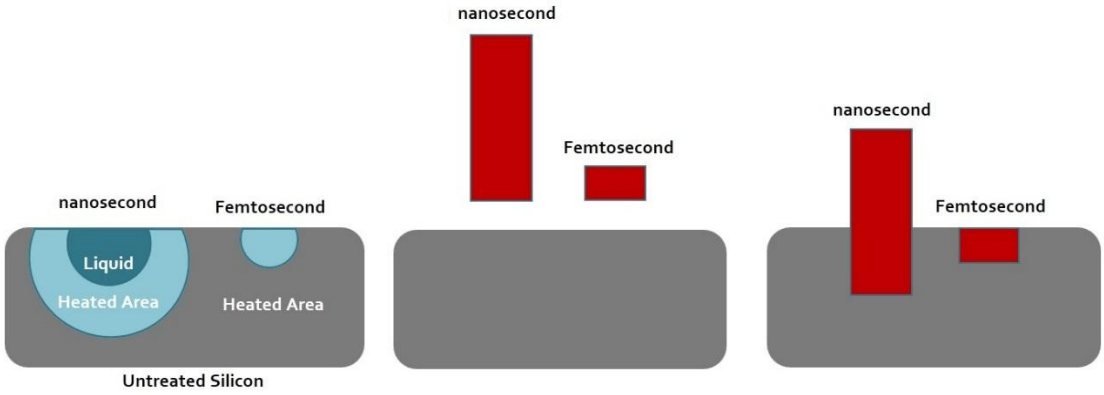

Fig. 2 Depiction of the heated regions and the difference in pulse duration between the nanosecond and femtosecond.

As cellular growth is highly dependent on surface characteristics, it is important to have a method that gives the ease of control over the patterns and features that can be implemented onto a material. As previously suggested, laser processing is an efficient and cost effective method to do so. Other processes aiming to roughen the surface such as sand blasting or acid etching may be inexpensive; however, their randomized process has shown that cell growth tends to occur equixially, leading to random bone cell orientations. In addition, many impurities are introduced by imbedded particles from the blasting process hence increasing the cytotoxicity of the material. Other methods such as ion or electron beam

texturing, although precise, require a vacuum. This not only increases cost but also limits the size, shape, and irregularities of the processed material [3].

1.4.4 Thin Film Deposition Methods

The addition of nanoparticles is another method for modifying the surface of substrates. Their applications have been seen in electronics, photonics, and bio-engineered devices [38]. Gold is the leading candidate in nano-sized electrical conductor modification [39]. Unlike other metals, it is one of the few elements that can be used at the nanoscale due to its resistance to oxidation. Metals such as silver and copper not only are not as biocompatible but they are highly reactive and would be consumed by oxidation at the nanoscale unless protected [40, 41]. Gold itself is a soft metal with a face centered cubic crystal structure. Although not as electrically conductive as silver, it has both better corrosion resistance and does not lead to the formation of cytotoxic elements in the body [39, 42]. When Gold is broken down into nanoparticles, the metal behaves differently. The crystal structure of Gold nanoparticles with diameters of less than 10 nm is no longer agreed upon as being face centered cubic and instead a variety of different forms are predicted [42]. This helps explain some of its new key properties including its high surface-to-volume ratio, excellent molecular-recognition, and high surface energy [43, 44]. The unique chemical and physical properties of Gold nanoparticles help transfer electrons from the biospecific layer to the electrode surface in many applications [43]. They have also been seen to increase the sensitivity of biochemical detection of electrochemical biosensors [45]. Research has shown that increases in the size of the Gold particle increases the sensitivity of certain sensors up to a limit [44]. The distances and sizes of these particles also cause changes in the energy distribution through the material [24].

The reduction of Gold into the nanoscale also affects its melting point. As a bulk material, Gold will melt around 1068℃, whereas nanoparticles of the material will have a lower melting point due to the significant increase in surface area. Measurements taken for melting points of Gold particles in the 5 nm diameter range were measured at 830℃, and by 1 nm the particles liquefy around 200℃ [42].

It is also important to note the occurrence of quantum effects affecting the conductivity of the substrate contacting the Gold. Classically, an insulator placed between a tiny gap separating the two Gold atoms would not allow current flow. At the nanoscale, the physical dimensions of the objects in play approach those of quantum quantities. This creates a probability that applying a voltage between the two separated conductors will allow for current flow as the electrons "tunnel" through the small gap [42, 46, 47]. The next phenomenon that occurs at the nanoscale is caused by an electron that has tunneled from one Gold particle to the next. At that point in time, the particle in question has a negative charge until it tunnels to the next electrode. This causes it to have a negative charge, thus repelling any other electrons from tunneling to that specific particle and causing a halt in the current flow. Only an increase in voltage high enough to overcome the repulsion of the electron can re-establish the flow. This causes an inhomogeneous current flow composed of the tunneling effect and what is known as the Coulomb blockade. This phenomenon is referred to as the Coulomb staircase [42].

The main downside to micro and nanoporous Silicon is its low conductivity as compared to the original substrate [48], making the addition of these nanoparticles an attractive solution. The addition of nanoparticles can be achieved through various methods, most commonly through physical or chemical deposition. Chemical deposition can be done in a

number of ways, including, but not limited to Chemical Vapor Deposition (CVD) and plating techniques [49]. These methods undergo a process of submersion into a chemical fluid where a chemical reaction between the substrate and the latter results in an equally coated surface. CVD requires the substrate to be placed into a pressurized chamber with a specific organometallic gas which will react with the substrate or dissolve over its surface into a uniform layer. Plating on the other hand requires a chemical bath containing the metal salts required for deposition, also resulting in a uniform coating. The thickness of the film can be estimated based on the time for which it is submerged. The addition of an electrical current to the substrate, known as electroplating, can help speed up the process and offer more controllability [49].

Physical deposition techniques on the other hand are generally achieved through either sputtering or evaporation. Unlike chemical deposition, they do not rely on chemical reactions and instead form thin films through mechanical or thermodynamic methods controlled by low-pressure and vacuum environments [50]. Physical Vapor Deposition (PVD) by vacuum evaporation is attained through the atomic deposition of the vaporized material onto the substrate. A phase change from solid to vapor state and back again to solid causes the formation of a coating. The material is thermally vaporized through electrical heating or using an electron beam. PVD by sputtering is commonly used in SEM applications where the coating provides an electrically conductive thin film on the surface to inhibit the effect of charging from the electrons and enhance the emission of secondary electrons. It also reduces the potential of thermal damage to the specimen. Sputter coating normally requires a noble gas such as Argon, which is admitted into a pressurized chamber through a leak valve. This allows for the formation of a glow discharge between an anode

and a cathode. In most cases, Gold acts as the cathode and the sample to be sputtered acts as the anode, where the free ions and electrons from the inert gas are attracted to opposite electrodes and form a small current. Increases to the voltage cause collisions between the electrons and the gas resulting in ionization. Once the voltage across the gas tube is larger than the breakdown potential, a self-sustaining glow discharge formation occurs. For this to remain self-sustaining, the electrons need to be regenerated through the positive ion bombardment of the cathode, causing erosion of the cathodic material onto the surface of the sample. Thick coatings using a sputtering technique cannot be achieved and deposition of a uniform layer is difficult to attain on complex shapes [50]. This technique however does not require specialized precursor materials as necessitated by chemical deposition. It also has a wide variety of different materials available for deposition.

Overall, CVD processes normally require much higher temperatures compared to physical deposition methods, placing the requirement of a high thermal capacity on the substrate [49]. Not only that, but physical deposition techniques do not require some of the harsh and toxic chemicals used in chemical deposition.

1.5 Silicon

Having four valence electrons covalently shared in its pure state, Silicon is highly affected by impurities and dopants added to its diamond crystal lattice. Silicon can be classified into a p or n-type semiconductor depending on the impurities present. These foreign atoms affect the electrical properties of a semiconductor [51, 52]. N-type semiconductors are generally doped with impurity atoms having five valence electrons, causing the contribution of an extra electron able to vastly increase the conductivity of an intrinsic semiconductor. Impurities such as Antimony, Arsenic, or Phosphorous are examples of

doping contents able to act as electron donors. This causes the electron energy levels to be nearer the top of the band gap making them easily excitable into the conduction band. P-type semiconductors on the other hand have three valence electrons, thus causing the formation of a “hole”. These holes are deficiencies of valence electrons and can be achieved through the addition of impurities such as Boron, Aluminum, or Gallium. The electron deficiencies created in the band gap cause excitations in the valence band electrons [52].

Intrinsic semiconductors exhibit electron movement and when crossing the band gap, will leave behind vacancies or holes. This occurs at temperatures above absolute zero, and when an external voltage is further applied both electrons and holes can be moved contributing to the current flow. As the movement occurs, electrons move from one lattice position to another, filling hole vacancies. At temperatures above absolute zero, some of the covalent bonds held by the electrons are broken, resulting in conduction electrons which can carry electrical current. In Silicon, approximately 1.1eV is required to induce a hole and a conduction electron. Band theory can be used to model the conductivity of a semiconductor, where it is suggested that at common temperatures electrical conductivity can occur with the finite possibility that electrons will reach the conduction band [52].

It is important to introduce the concept of the Fermi level. This level is the maximum height electron energy levels can reach at absolute zero. It can also be thought of as the electrons chemical potential. In intrinsic semiconductors, the Fermi level lies approximately half way between the conduction and valence band. The addition of a dopant results in the Fermi level moving closer to either of the bands. Temperature also plays a role in the Fermi level, where higher temperatures encourage more electrons to exist above the Fermi level.

The Fermi function describes and estimates the electron energy state occupied at a given temperature. In semiconductors, higher temperatures induce higher fractions of electron flow past the gap leading to a higher conduction. Fermi energy can also describe the velocities of electrons participating in conduction, namely the ones closest to this energy [52].

1.6 Osseointegration

The structural and functional bond occurring between an implant and a bone is formed through the process of osseointegration, where the adsorption of proteins leads to cell adhesion, growth, and differentiation. Osteoblast cells fill the voids and proliferate between the implant surface and existing bone. These cells act as a founding layer for future mature bone cell formation. The adsorption of protein and attachment of osteoblast cells is highly dependent on the surface chemistry and topography of the materials, hence the importance of proper surface modifications. The formation of nanoscale surface features can not only increase the overall surface area allowing for more attachments, but it can also affect cell adhesion, proliferation, and differentiation through protein interactions. The protein complexes attaching cells to the surface are affected by nanoscale features, causing changes in the microfilaments and microtubule attachments forming the focal adhesion complexes. At a microscale, features such as grooves, ridges, and mountains not only have similar effects to nanoscale features, but they are able to guide and organize cells. Previous studies have found that linear grooves formed on the surface can lead to organized regrowth and hence a minimization in scar tissue during healing. Through these surface features, cells can be made to elongate, contract, align, and organize in certain manners. Macroscale

features on the other hand tend to affect the direct attachment of the bone to the implant and increase its longevity through slots, dimples, and threads [3].

1.7 Research Objectives

The affordability, efficiency, biocompatibility, and accessibility of the materials currently in use such as stainless steel, Gold, Titanium, and Silver are still being researched; however, materials with better performances are appearing [1]. Silicon is one of these materials, and although non-biocompatible in its pure form, can be processed using various techniques to form porous and biocompatible structures. This research proposes an efficient, and cost effective method to process Silicon into micro and nanocomposites (Si/Au) using an Nd:YAG nanosecond pulsed laser system. The conductivity will be controlled using two different methods and these will be compared to determine the most effective. It will involve the processing of Silicon wafers: (1) a single crystalline Silicon wafer with Gold sputtered on its surface for either four or eight minutes and (2) a thin film Gold coated wafer. These will be laser ablated at different powers and scanning parameters, and their surface topography investigated. The effects of each of these approaches will be analyzed. The purpose of this study will be to develop and propose a novel method to generate Gold coated or sputtered nanofibers on the surface of Silicon using a nanosecond pulsed laser to customize its electrical and biocompatibility properties to further improve its viability in sensing applications.

The main objectives of this project are listed as follows:

- Determine the feasibility of generating nanofibrous structures using a nanosecond pulsed laser.

- Investigate the effects of laser parameters on nanofibrous structures, material, and physical properties.
- Study the effects of scanning parameters (overlaps, power, and line spacing) on Silicon.
- Combine Gold sputtering techniques with laser processing for its potential use in sensor fabrication.
- Laser process a thin film Silicon Gold wafer and compare its properties to that of Gold sputtered Silicon for its potential use in sensor fabrication.

Chapter 2

2.0 Physical Modelling

A number of mathematical models and equations were utilized in this research to qualitatively assess some of the key parameters applied throughout the study. These have been customized to fit the desired standards applied in this experiment. The temperature, evaporation, and plasma pressure are all modeled to aid in the explanation of the formation of nanoparticles and to offer theoretical confirmations.

2.1 Temperature

The temperature model in question has been used in a similar study by Colpitts et al. to determine surface temperatures [53]. It has since been customized and applied for the specific parameters used in this research. A one-dimensional heat equation derived for its specific use in laser ablated regions is applied to estimate the quantitative trends expected to be seen when a variation in scanning parameters is applied.

Defining the heat energy in a subregion as in Eq. 2, we know that the rate of change of this energy is equal to the heat energy into the three-dimensional subregion, V, in addition to the heat energy generated within the solid per unit time. This can be written in integral form, where c_p is the specific heat, ρ the materials' density, T the temperature, $\emptyset$ the vector heat flux, and Q the heat energy generated per unit time. Since we are aiming to calculate

the heat flux through the subregion V, the normal component of the heat flux is taken by multiplying it by the unit vector $\hat{n}$, as seen in Eq. 3 [54].

$$Heat\ energy = \iiint_V\ c_p \rho T\ dV \qquad \textbf{Eq. 2}$$

$$\frac{d}{dt}\iiint_V\ c_p \rho T\ dV = -\iint_S\ \emptyset \cdot \hat{n}\ dS + \iiint_V\ Q\ dV \qquad \textbf{Eq. 3}$$

Assuming the flux is a continuously differentiable vector field, and using the divergence theorem, we have

$$\iint_S\ \emptyset \cdot \hat{n}\ dS = \iiint_V\ \nabla \cdot \emptyset\ dV \qquad \textbf{Eq. 4}$$

Leaving us with

$$\iiint_V\ \left(c_p \rho \frac{\partial T}{\partial t} + \nabla \cdot \emptyset - Q\right) dV = 0 \qquad \textbf{Eq. 5}$$

Since the integral is assumed continuous and equal to zero for any arbitrary volume V, we are now left with [54]

$$c_p \rho \frac{\partial T}{\partial t} + \nabla \cdot \emptyset - Q = 0 \qquad \textbf{Eq. 6}$$

Thermal evaporation is an important factor in the formation of nanoparticles and nanofibers. Through the heating of the surface, particles and atoms are excited and ejected into the laser plume. The three-dimensional generalization of Fourier's Law of Heat Conduction can be written as [54]

$$\emptyset = -k_0 \nabla T \qquad \textbf{Eq. 7}$$

Where k_0 is the thermal conductivity and when divided by the specific heat and density will result in the thermal diffusivity, k. This equation relates the local heat flux density to the materials conductivity and the temperature gradient. In its differential form, it is important to note that in an anisotropic material such as laser-processed Silicon, the thermal

conductivity will vary with the orientation. The conductivity is also able to vary based on its spatial location in a non-uniform material, however this model considers these parameters as constant for simplicity. Incorporating Fourier's Law now results in [54]

$$\frac{\partial T}{\partial t} = k\nabla^2 T + \frac{Q}{c_p \rho} \qquad \textbf{Eq. 8}$$

Setting the problem in one dimension, we can solve for a general solution as:

$$\frac{\partial T}{\partial t} = k\frac{\partial^2 T}{\partial x^2} + \frac{Q}{c_p \rho} \qquad \textbf{Eq. 9}$$

For simplicity, a rectangular shaped laser pulse profile with a step-like rise and fall in time is taken. This defines Q as zero since there is no heat source within the Silicon, and the intensity I, where $I = I_a(0 \leq t \leq t_p)$, t_p the laser pulse duration, and I_a the absorbed laser intensity as detailed in Eq. 13. The laser target is assumed only in the x-axis with $x \geq 0$, and the heat flux at the target surface equal in temporal form as the absorbed laser heat flux. It is also assumed that the laser energy is absorbed into a layer much thinner than the penetration depth of the heat wave, that a single laser pulse heats the target, losses due to radiation and plume expansion are ignored, and that the density, conductivity, and specific heat are held constant. With these suppositions in place, the Landau Lifschitz solution solves this one-dimensional heat problem assuming an infinite inhomogeneous bar with a heat source, where the unit heat is instantaneously applied at time τ and position y [55]. Using Fourier transforms, inverse Fourier transforms, the superposition integral, and the previously stated assumptions, the solution to the heat conduction equation can be written as [56]

$$T(x,t) = \frac{k^{1/2}}{k_0 \pi^{1/2}} \int_0^{t_p} \frac{I_a(\tau)}{(t-\tau)^{1/2}} exp\left\{-\frac{x^2}{2k(t-\tau)}\right\} d\tau \qquad \textbf{Eq. 10}$$

Averaging Eq. 10 above by taking its integral through space at the end of the laser pulse can be written as [56]

$$\langle T \rangle = \frac{1}{(kt)^{1/2}} \int_0^{\infty} T(x, t_p) dx \qquad \textbf{Eq. 11}$$

Now writing it in its explicit form after the end of the laser pulse leads to Eq. 12. It should be noted that the maximum target temperature occurs at the end of the laser pulse $T_m = T(0, t_p)$ assuming the target is heated by a single pulse [56, 57].

$$T(0,t) = T(0,t_p)\left(\frac{t_p}{t}\right)^{1/2} = \sqrt{\frac{2}{\pi}} \frac{I_a (k t_p)^{1/2}}{k_0} \left(\frac{t_p}{t}\right)^{1/2} \qquad \textbf{Eq. 12}$$

Using Eq. 13 below, Eq. 12 can be simplified into Eq. 14 [57].

$$I_a = K(1-R)\frac{4P}{\pi d^2 t_p f} \qquad \textbf{Eq. 13}$$

$$T(0,t_p) = \sqrt{\frac{2k}{\pi^3 t_p}} \frac{4K(1-R)P}{k_0 f d^2} \qquad \textbf{Eq. 14}$$

Since the maximum temperature is reached at the end of the laser pulse, it is assumed that the minimum temperature occurs at the beginning of the laser pulse, or at $T_{min} = \beta T_m$, where β is now defined as a constant ratio of the square root of the frequency multiplied by the pulse duration ($\beta = \sqrt{t_p f}$). The maximum and minimum temperature from one to *n* pulses can be calculated through β and a geometric series as [57]

First pulse: $(T_{max})_1 = T_m$; $(T_{min})_1 = \beta T_m$ **Eq. 15**

Second pulse: $(T_{max})_2 = (1+\beta)T_m$; $(T_{min})_2 = \beta(1+\beta)T_m$

*n*th pulse: $(T_{max})_n = (1+\beta+\beta^2+\beta^3 \ldots + \beta^{n-1})T_m$;

$$(T_{min})_n = \beta(T_{max})_n \quad = [(1-\beta^n)/(1-\beta)]T_m$$

Averaging this starting from the beginning of the laser pulse to its end including the pulse interval leads to an equation where the surface temperature average for an *i*th laser pulse can be determined as [57]

$$\bar{T}_i = \frac{1}{t_p + t_{pp}} \int_0^{t_p+t_{pp}} T_{m,i}(0,t)dt = 2\beta T_{m,i} \frac{1-\frac{2}{3}\beta}{1+\beta^2} \qquad \textbf{Eq. 16}$$

This equation can then be furthered to determine the surface temperature after several *n* pulses. By replacing $T_{m,i}$ with the geometric equation of $(T_{max})_n$, the average surface temperature can be estimated as [57].

$$\overline{T_n} = 2\beta \frac{\left[1-\frac{2}{3}\beta\right]}{(1+\beta^2)} \frac{T_m}{(1-\beta)} \left[1 + \frac{\beta^n - \beta}{n(1-\beta)}\right] \qquad \textbf{Eq. 17}$$

Although many assumptions are made to achieve these calculations causing higher temperature values than expected, the relation between the surface temperature with respect to the overlaps and line spacings can be observed and compared to phenomenon's occurring in the experimental results achieved [57]. The theoretical surface temperature calculations are conducted using Matlab, with the code outlined in the Appendix.

2.2 Evaporation Rate

Equations pertaining to the evaporation rate were customized for this research project and applied in order to model and theoretically represent the increase in particles ablated from the material that are later able to rearrange into new structures. It is dependent on several

parameters, including the surface temperature modeled above. A one-dimensional model is used in this scenario to model surface evaporation in the upward direction.

Thermal evaporation is assumed to begin sometime after the equilibration time is reached ($t > t_{eq}$). After this time limit, the temperature begins to descend following the linear heat conduction law. The evaporation rate can be simplistically derived by equating the kinetic energy with the absolute temperature and the density of air. Since this occurs at the solid-air interface, air is assumed to play the role of saturated vapor as an ideal gas and the thermal evaporation rate is estimated according to Eq. 18 [58]. This equation assumes a one-dimensional model and a Maxwell distribution.

$$\langle R_{evp} \rangle_{therm} \cong n_{air} \left(\frac{k_B T_{max}}{2\pi M_a} \right)^{\frac{1}{2}} \left(t_p t_{eq} \right)^{\frac{1}{2}} \left[\frac{atoms}{cm^2} \right] \qquad \textbf{Eq. 18}$$

To determine the number of evaporated atoms from the same spot after successive pulses, the maximum temperature estimation equation was used once more. From Eq. 14, one can solve for T_{max} to obtain [58]

$$T_{max} = \frac{2 I_a \left(k t_p \right)^{1/2}}{k_0 \pi^{1/2}} \qquad \textbf{Eq. 19}$$

The laser intensity on the target surface is obtained by multiplying the intensity of incident pulse by the laser absorption coefficient ($I_a = \alpha I_0$). Using the lasers average power, the incident pulse intensity can be defined as [58]

$$I_0 = \frac{P_{avg}}{R_{Rep} t_p A_{foc}} \qquad \textbf{Eq. 20}$$

The average power is measured in watts, R_{Rep} being the laser repetition rate in Hz, and A_{foc} the area of the irradiation focal spot in cm^2. Placing equations 19 and 20 together, we obtain the maximum temperature as a function of laser parameters as follows [57, 58]

$$T_{max} = \frac{2\alpha P_{avg} k^{1/2}}{k_0 R_{rep} A_{foc} (\pi t_p)^{1/2}} \quad \textbf{Eq. 21}$$

Substituting this into the evaporation rate equation outlined in Eq. 18, we can now theoretically determine the rate for single pulse ablation [58].

$$\langle R_{evp} \rangle_{therm} = n_{air} \left(\frac{\alpha k_B k^{\frac{1}{2}} t_p^{\frac{1}{2}} t_{eq} P_{avg}}{M_a k_h \pi^{\frac{3}{2}} R_{rep} A_{foc}} \right)^{1/2} \left[\frac{atoms}{cm^2}\right] \quad \textbf{Eq. 22}$$

The rate can then be converted into atoms using the atomic mass of Silicon and the laser pulse dwell time D_t, leaving the average theoretical number of evaporated particles estimated as [58]

$$N_{MP} = R_{evp} R_{rep} A_{foc} D_t \; [atoms] \quad \textbf{Eq. 23}$$

2.3 Plasma Pressure

A key step in laser ablation is the formation of the plasma plume. As the laser energy is absorbed by the material, the formation of a hot and dense plasma occurs. This in turn induces a mechanical impulse resulting from the plasma pressure generated at the surface. Increases in the plasma pressure will lead to deeper ablation depths. In the first step, the plasma pressure induces a shockwave during the laser pulse duration, which in turn propagates into the target material. As the laser pulse ends, the pressure is maintained in the plasma, however with a decreasing tendency during the adiabatic cooling. The mechanical impulse has momentum at this stage caused by the shockwave.

This model assumed that two shock waves occur within the target and surrounding gas due to the plasma, that the shock wave impedances are constant, and that the medium of ablation is a perfect gas. The plasma pressure during the heating phase of the pulse can be theoretically determined according to the equation derived by Fabbro et. al. [59]. We begin

with the thickness of the interface $L(t)$ at time t, where the interface wall displacement results only from the fluid motion between the two propagating shock waves. This leads to the mathematical description of Eq. 24, where $u_i(i = 1,2)$ denotes the two fluid velocities behind each shock wave [59]:

$$L(t) = \int_0^t [u_1(t) + u_2(t)]dt \quad \textbf{Eq. 24}$$

The shockwave relation to determine the plasma pressure P can be written as a function of the density ρ_i, the shock velocity D_i, and the shock impedance of the material Z_i [59]:

$$P = \rho_i D_i u_i = Z_i u_i \quad \textbf{Eq. 25}$$

Now assuming constancy of the shock wave impedances with $Z_i = \rho_i \cdot D_i$, and using equations 24 and 25 we have [59, 60]:

$$\frac{dL(t)}{dt} = \frac{2}{Z}\, P(t) = P(t)\left(\frac{1}{Z_1} + \frac{1}{Z_2}\right) \quad \textbf{Eq. 26}$$

The plasma thickness dL increases through the absorbed laser energy during the time interval dt. The laser energy being deposited per unit surface area $I(t)dt$ and absorbed results in increases to the internal energy in Joules per unit volume $E_i(t)$ by $d[E_i(t)L]$. This allows for the conservation of energy to be written as follows [59, 60]:

$$I(t) = P(t)\frac{dL}{dt} + \frac{d[E_i(t)L]}{dt} \quad \textbf{Eq. 27}$$

Considering only a fraction α of the internal energy is related to the thermal energy $E_T(t)$, then the pressure can be related to the thermal and internal energy for an ideal gas as follows [59]:

$$P(t) = \frac{2}{3}E_T(t) = \frac{2}{3}\alpha E_i(t) \quad \textbf{Eq. 28}$$

Substituting into Eq. 27 yields [59]:

$$I(t) = P(t)\frac{dL(t)}{dt} + \frac{3}{2\alpha}\frac{d}{dt}[P(t)L(t)] \quad \textbf{Eq. 29}$$

Now using the above equations and assuming a constant laser intensity, a laser pulse duration of t_p, and initial condition $L(0) = 0$, one can obtain a constant pressure equation in kilo bars during the duration of the laser pulse as follows [59, 60]:

$$P_{pressure} = 0.1\left[\left(\frac{\alpha}{2\alpha + 3}\right) Z I_0\right]^{0.5} \quad \textbf{Eq. 30}$$

Now estimating I_0 as in Eq. 31 and substituting into Eq. 30 results in Eq. 32 [59, 60].

$$I_0 = \frac{4P_{power}}{\pi d^2 t_p f} \quad \textbf{Eq. 31}$$

$$P_{pressure} = 0.1\left[\left(\frac{\alpha}{2\alpha + 3}\right)\frac{4ZP_{power}}{\pi d^2 t_p f}\right]^{0.5} \quad \textbf{Eq. 32}$$

The interface thickness in micrometers can also be obtained from the above derivations as [59, 60]

$$L(t_p) = \frac{2 * 10^4 P_{pressure} t_p}{Z} \quad \textbf{Eq. 33}$$

2.4 Electrical Conductivity

The electrical conductivity of the Silicon and Gold composite needed to be explained, especially considering the size of the conductive particles that are dealt with in this research. Due to the very small nature of the Gold and Silicon particles, quantum theory is to be applied. The following equations offer explanation as to the expected trends in the conductivity of the substrate based on particle distances and sizes.

Assuming the particles are of a spherical shape and the Silicon dioxide matrix is insulating, then the volume fraction can be determined as in Eq. 34, where R_c is the conductive particle

(Au) radius, R_i the insulating particle (SiO_2) radius, and n_c and n_i the number of conductive and insulating particles respectively [46].

$$P = \frac{n_c R_c^3}{n_c R_c^3 + n_i R_i^3} \quad \textbf{Eq. 34}$$

The theoretical interparticle distances, l, assuming spherical conductive particles and a uniform size distribution can be determined using the volume fraction of the conductive phase described above [46].

$$l = R_c \left[\frac{4\pi}{3P}\right]^{1/3} - 2 \quad \textbf{Eq. 35}$$

The interparticle distance can then be related directly to the conductivity of the Silicon dioxide σ_i and Gold particles σ_c as in Equation 36 below [61].

$$\sigma_i = \sigma_c e^{-2X_t l} \quad \textbf{Eq. 36}$$

Where is X_t defined as in Equation 37, with *m* being the mass of the charge carriers, $V(t)$ the temperature modified barrier height, and *h* Planck's constant.

$$X_t = \left[\frac{8\pi^2 m V(t)}{h^2}\right]^{0.5} \quad \textbf{Eq. 37}$$

Assuming constancy of the parameters in X_t, the effect on the conductivity of the Silicon dioxide becomes highly dependent on the distance between the conductive particles. As one would expect from the equations, higher numbers and larger particle radii of conductive particles results in a higher volume fraction, which in turn results in increases in interparticle distances.

The conductivities of Silicon dioxide have been measured and investigated in the past, showing promising results for its use in electronic applications. One study has shown that thermally grown Silicon dioxide on n-type Silicon had a higher AC conductivity than p-

type [62]. As Silicon is processed to become porous, an increase in the Oxygen content occurs, however a reduction in the overall conductivity. A previous study was conducted on n-type <111> Silicon that had been chemically etched to form porous Silicon oxide to determine the effects of conductivity. It was found that the latter decreased by almost an order of magnitude when conducted in dry atmosphere [62]. This suggests that the conductivity may be affected by biological mediums. The degree of oxidation has been seen to have a direct effect on the conductivity, affecting it up to a factor of 10^9 by varying the composition of SiO_x, where x varies between 1.5 and 2 [63].

Chapter 3

3.0 Experimental Setup and Procedure

The first approach involved the laser processing of single crystalline Silicon wafer <100> at an average power of 12 W, at line spacings of 0.025 mm, 0.1 mm and 0.15 mm, and at either one, three, or five overlaps. The line spacing refers to the space between each successive line pulsed by the laser, measuring from the center of the laser beam. The overlaps denote the number of pattern repetitions made on the surface of the Silicon. These were Gold sputtered for either four or eight minutes. As shown in Fig. 3, the Silicon wafer is laser processed, then Gold sputtered and analyzed through various characterization techniques.

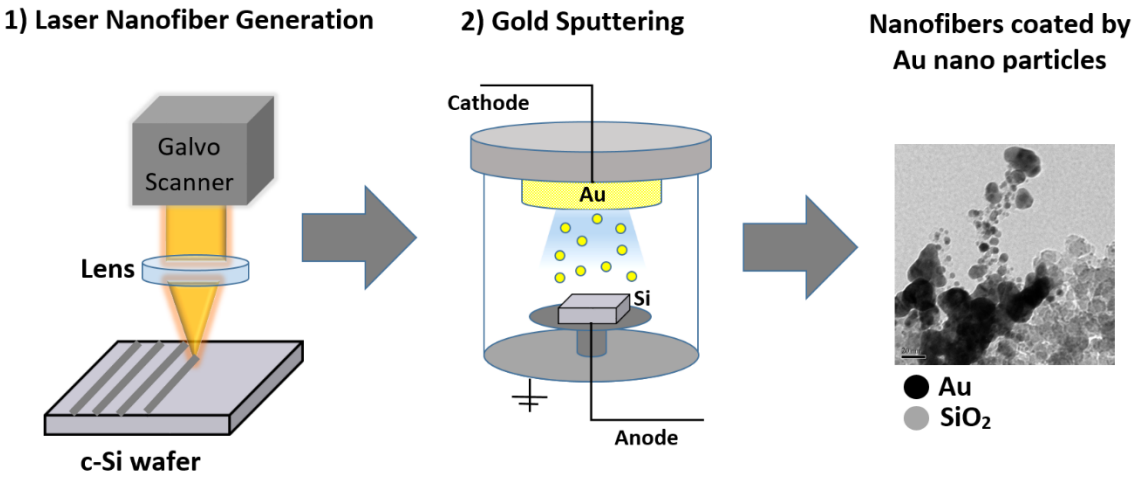

Fig. 3 Approach I: Gold sputtering of laser generated Silicon dioxide nanofibers.

The second approach involved processing Gold-coated single-crystalline Silicon wafers <Au1000> at different powers and overlaps as shown in Fig 4. Sets of samples were made

at 2.35 W, 4 W, 9W, and 12W at a line spacing of 0.025 and 0.01mm, at both one and five overlaps. The scanning speed and frequency of the laser was kept constant at 100 mm/s and 100 kHz respectively for all samples.

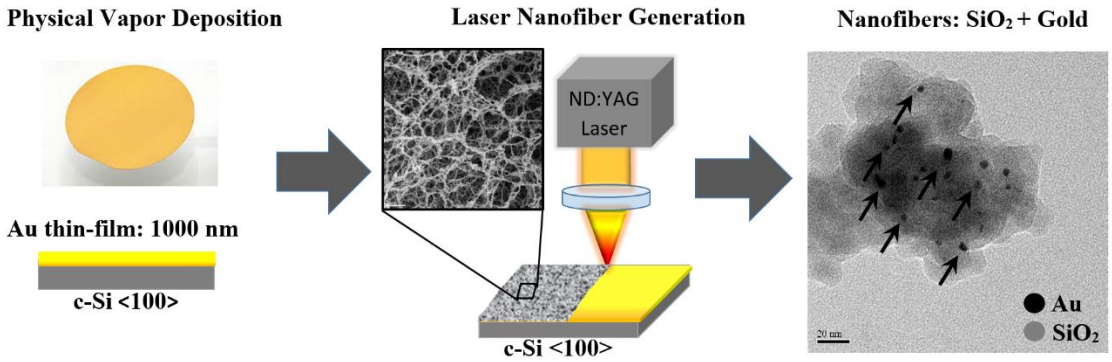

Fig. 4 Approach II: Laser processing of Au-coated (1000 nm) Si wafers.

3.1 Laser Processing

An Nd:YAG pulsed laser with a wavelength of 1064 nm was used on both a single crystalline and an evaporated Gold Silicon wafer (Au 1000) for this experiment. The circular output beam of the laser has a diameter of 9 mm and is reduced to 8 mm using an iris diaphragm before entering an XY galvanometer scanner (JD2204 by Sino-Galvo). This scanner has an aperture of 10 mm and a beam displacement of 13.4 mm. A scan lens with a focal length of 63.5 mm was used to control the focus of the laser on the sample surface, resulting in a theoretical laser spot diameter of 20 µm. EZCAD software was used to control laser parameters, *e.g.*, to specify scanning speeds, overlaps, frequency, and line patterning. The overall setup can be seen in Fig. 5 below. Simple line patterns at an orientation of <100> were made on the samples at varying powers, namely 2.35 W, 4 W, 9 W, and 12 W. The line spacing was also varied with certain samples at 0.01 mm, 0.025

mm, 0.05 mm, 0.1 mm, and 0.15 mm. Overlaps of the line pattern were made for one, three, and five loops.

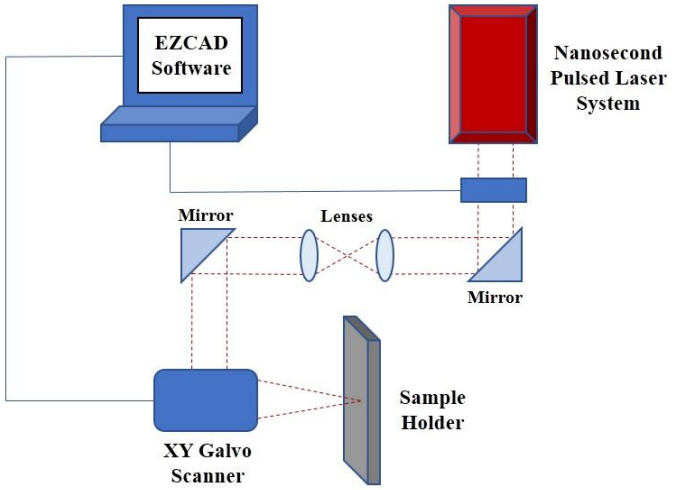

Fig. 5 Experimental setup of the Nd:YAG laser system.

3.2 Microscopy and Surface Characterization

3.2.1 Scanning Electron Microscope (SEM)

A variety of means were employed for surface characterization, including the use of an SEM to image the surfaces of the Silicon samples. This imaging technique employs a high-vacuum to prevent electrical discharge as well as to reduce impedance on the travelling electrons. The electrons striking the surface of the specimen are reflected, and an energy alteration occurs. They are then collected at a detector and the electrical energy converted, amplified, and refined before a projection results. Imaging was conducted at the UNB Microscopy and Microanalysis Facility using a JEOL JSM-6400 Scanning Electron Microscope mounted with an EDAX Genesis 4000 Energy Dispersive X-Ray (EDS) analyzer. Both EDS and SEM were conducted at an accelerating voltage of 15 kV.

3.2.2 Sputter Coater

An Edwards S150A sputter coater was used for the Gold sputtering of the samples at the UNB Microscopy and Microanalysis Facility. This machine is fitted with a Gold cathode and the overall thickness is dependent on the gas flow (Argon in this case), voltage, and discharge duration. Using Eq. 38 below, the thin film layer T, in the order of nanometers, can be estimated based on the properties of the sputtering machine which include the measure of gas flow controlled by the current *I* in milliamps, *keV* the voltage setting in kilo electron volts, *t* the discharge duration in minutes and a constant, *K*, which is taken to have a value of five for the Argon/Gold combination of this model.

$$T = I \times t \times K \times keV \qquad \textbf{Eq. 38}$$

3.2.3 Transmission Electron Microscope (TEM)

Similarly to the SEM, the TEM requires both a vacuum and images through the use of an electron beam. The main difference is that a very thin slice of the specimen must be utilized as the electrons are made to pass through to give a higher magnification. Some electrons are passed through unaffected, others may be absorbed, and finally some areas may deflect the electrons causing them to scatter. A JEOL JEM-2010 Scanning Transmission Electron Microscope adapted with a Gatan Ultrascan camera using Digital Micrograph was used to collect the desired images. Imaging and analysis were conducted at an accelerating voltage of 200kV.

3.2.4 Field Emission Scanning Electron Microscopy (FESEM)

The FESEM can be used to image the entire specimen at a higher resolution and clarity than the SEM. The FESEM model used was the Hitachi SU-70 Field Emission Gun (FEG)

SEM. THE FEG SEM was mainly used to image at a higher resolution than the SEM for our Gold-coated samples, which were not sputtered prior to being imaged.

3.2.5 Micro-Raman Spectroscopy

The chemical composition of processed Silicon was characterized using a Renishaw inVia micro-Raman spectrometer having a maximum power of 150W. Micro-Raman spectroscopy offers a non-invasive, simple, and rapid method to analyze nanoscale materials [64].

3.2.6 Energy Dispersive X-ray (EDX)

EDX was used in conjunction with the SEM, TEM, and FESEM to determine the chemical composition, concentration, and the elements present on the samples surface. This was especially important for monitoring the levels of Gold and presence of Oxygen. An EDAX Genesis 4000 Energy Dispersive X-Ray analyzer was used at an accelerating voltage of 15 kV.

3.3 Light Spectroscopy

The STS-NIR Spectro Radiometer (Ocean Optics, Dunedin, Florida, USA) was used to determine the optical properties of the samples, namely to measure the reflectivity coefficient of the samples at varying overlaps and line spacing for comparative purposes at wavelengths of visible light between 175 and 885 nm and an optical resolution of 1.5 nm.

3.4 Impedance Spectroscopy

A CH Instruments Inc. (USA) model 760 potentiostat was used to measure the conductivity of the processed Silicon samples using AC impedance spectroscopy. The samples were

connected via alligator clips to the spectrometer (two-electrode mode) and measurements were obtained at frequencies between 0 and $1 \cdot 10^6$ Hz and at the potential amplitude of 10 mV.

3.5 Image Analysis

The software ImageJ 1.501 by Wayne Rasband at the National Institutes of Health, USA is used to determine particle and fiber diameters. It allows for the manual import and measurement of the features captured by TEM images.

3.6 Biocompatibility

The ability of bone to bond to a material is generally tested using a Simulated Body Fluid (SBF) solution. This solution mimics human blood plasma in terms of its ion concentrations. The adhesion of apatite on the surface of the material being tested allows for a useful prediction of its *in vivo* bone activity [65]. This biocompatibility test is conducted within the lab with the SBF prepared using the ingredients outlined in Table 1. Samples are submerged in the solution for a period of five weeks at a constant temperature of 36.5°C.

Table 1: Ingredient list for preparation of SBF [65].

Ingredients	Amount
NaCl	8.035g
$NaHCO_3$	0.355g
KCl	0.225g
$K_2HPO_4 - 3H_2O$	0.231g
$MgCl_2 - 6H_2O$	0.311g
1.0M - HCl	39mL
$CaCl_2$	0.292g

Na_2SO_4	0.072g
TRIS	6.118g
1.0M - HCl	0 – 5mL

The formation and adhesion of elements such as Calcium, Oxygen, Phosphorous, and Chlorine on the surface of the specimens will determine the biocompatibility. These will be characterized using some of the above-mentioned methods.

3.7 Statistical Analysis

Statistical analysis was carried out using Minitab® to ensure significance of the results. A confidence interval of 95% ($\alpha = 0.05$) was utilized along with a Tukey comparison method. Error bars indicate the standard deviation, and data with low statistical significance is clearly outlined. The null hypothesis (H_0) assumes no significant differences between the measured groups, while the alternative (H_1) indicates evidence of a statistical difference. A one-way ANOVA is used to compare and ensure statistical significance between the differently processed groups. All data presented in this report have shown statistical significance in terms of their differences unless otherwise stated.

3.7.1 Assumptions

Certain assumptions are made when conducting the experiment and measurements of the samples. In terms of the laser, these assumptions include the constancy of the ambient air in which the processing is occurring, and the laser focal point and diameter being the same for all the processed samples. It is also assumed that the impedance spectrometer runs current through the entirety of the sample. The sputtering conducted by the Edwards sputter coater is also presumed to evenly distribute the coating material.

Chapter 4

4.0 Generation of Nanofibrous Structures

Silicon samples were processed at one, three, and five overlaps at an average power of 12 W with line spacings of 0.025 mm, 0.10 mm, and 0.15 mm. SEM images were collected to determine the type of nanostructures present. Nanostructures have been shown to improve cellular interactions and modulate cell behavior. Nanofibrous structures are key in tissue engineering, where the scaffolds imitate the natural extracellular matrix [14]. Particles can be classified based on their sizes and are described by their structures. Microparticles are classified within a large range, however most are greater than 1 μm and smaller than 1000 μm. Nanoparticles are between 0.5 to about 50 nm, falling closer to the size range of certain individual atoms of 0.3 nm diameters [42]. Previous research conducted by Colpitts et. al. observed the formation of fibrous structures at the nanosecond pulse time [53]. This study focuses on evaluating the feasibility of their generation as well as explaining their formation in more depth in terms of changes in laser parameters, including but not limited to temperature, pressure, light absorption and particle sizes. The models outlined in previous sections are customized to help theoretically explain the nanofiber generation observed in this research.

Raman spectroscopy was also used to determine the chemical composition present in the processed Silicon. Fig. 6 below shows the results, where both amorphous and crystalline

Silicon are present alongside Silicon dioxide at a Raman shift of 500 cm^{-1}, 520 cm^{-1}, and 950 cm^{-1} [27, 64].

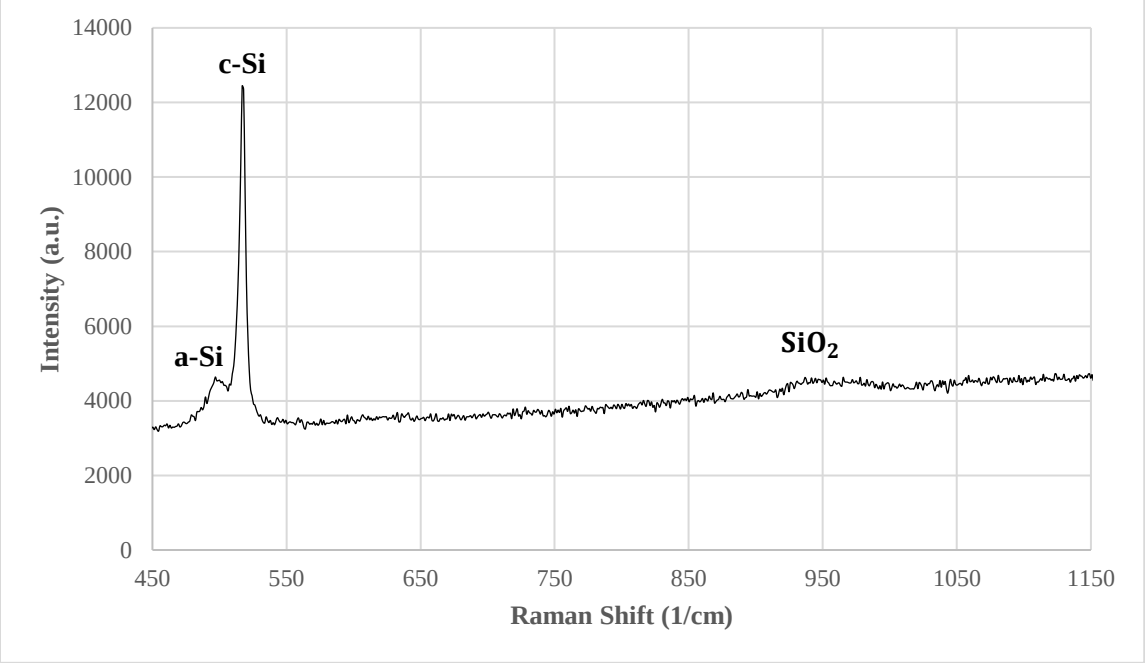

Fig. 6 Raman spectra of laser processed Silicon; a-Si: amorphous Silicon; c-Si: crystalline Silicon.

4.1 Line Spacing Effects

The effects of line spacing were clearly visible under the SEM. As seen in Fig. 7, increasing the line spacing resulted in the formation of microparticles with nanoscale porosity rather than nanofibers. The laser-ablated area is distinctly apparent in both (A) and (B) of the image below, as expected since the laser spot diameter is around 0.02 mm and much smaller than the designated line spacing. At 0.1 mm, microparticles form on the surface between the laser-ablated regions. Higher magnification reveals these microparticles to be formed of fine fibrous structures. At 0.15 mm, the microparticles are smaller and sparser, with a higher density of nanoparticles forming on the surface instead. The porosity of the nanostructures differs from the larger microparticles. The microparticles at the 0.15 mm

line spacing have a denser structure compared to the 0.1 mm sample. In theory, it is expected that an increase in laser plasma plume temperature will result in particle growth [35], as may be observed by comparing the images below. As the line spacing is decreased to 0.025mm, fibrous structures subdued. This means that the threshold temperature for the formation of nanofibers was reached, which is not generally expected at the nanosecond laser pulse time. At this power level and line spacing, the spot diameter was small enough such that the laser plume held an optimum temperature for the formation of these fibrous structures seen in Fig. 7 (C). Since the laser diameter is in theory approximately the size of this line spacing, little to no area is left that does not come into direct contact with the laser. This results in a more heated region and the plume density is kept stable for a longer period. This further increases the overall light absorption of the sample due to the change in topography. By creating a fiber network, the surface area increases and therefore all the mechanisms directly linked to the area are enhanced.

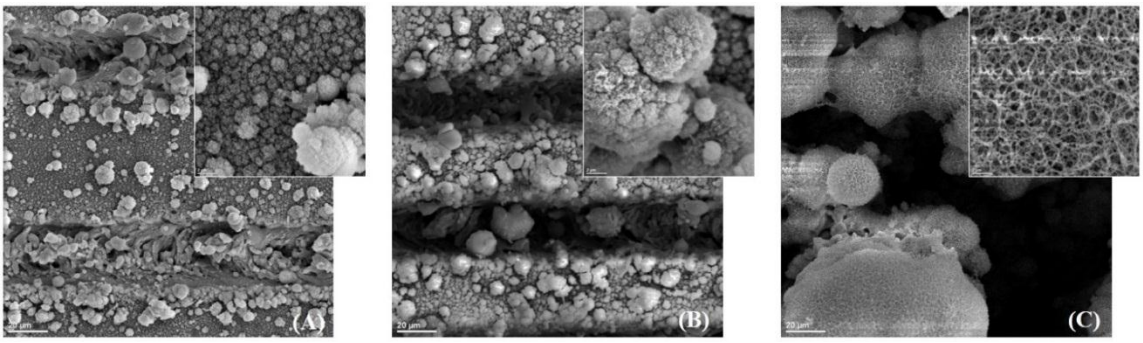

Fig. 7 SEM images of laser processed Silicon at five overlaps: (A) 0.15 mm, (B) 0.1 mm, (C) 0.025mm.

4.2 Overlap Effects

The next parameter observed was the effects of overlaps on the samples. Since micro and macroparticles are not of high interest to our study due to their reduced biocompatibility

compared to samples of higher porosities, the 0.025mm samples were analyzed more thoroughly.

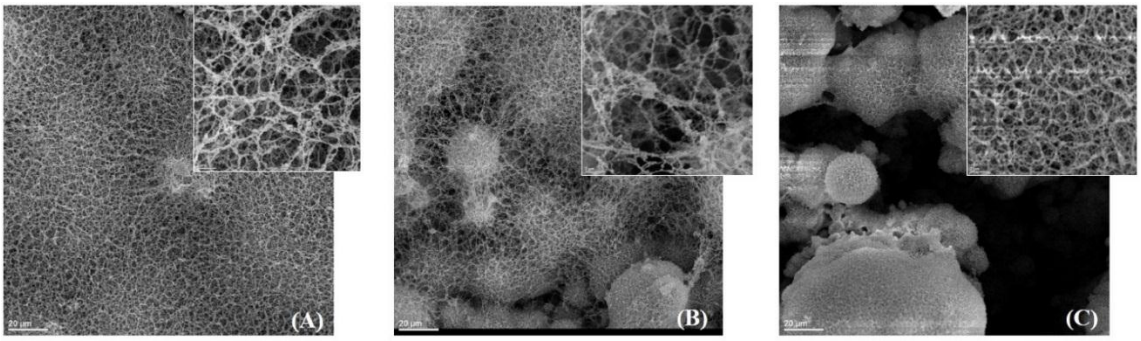

Fig. 8 SEM images of laser processed Silicon at 0.025 mm line spacing. (A) 1 OL, (B) 3 OL, (C) 5 OL. Scale: 20 **µm**.

The SEM images in Fig. 8 (A) show a uniform dispersion of interlinked nanofibers that form at a line spacing of 0.025 mm. When the overlap number is increased to three (B), small clusters of nanofibrous particles begin to form. By the fifth overlap (C), clear clusters of nanofibrous structures form with spaces between them. Again, increasing overlap is expected to increase particle growth because of increased temperature and light absorption. An increase in fiber diameter was also observed with increasing overlaps. The smallest fiber diameter—an average of 75 nm—was observed at one overlap. The increasing overlaps result in a denser plume therefore causing more particle collisions and hence larger agglomerates. Literature indicates that nanoporous structures increase the biocompatibility of the material by affecting the topology and cell scaffolding [66].

Furthermore, the mean roughness was measured for samples processed at a line spacing of 0.025 mm and at different overlaps. As can be seen in Fig. 10, increases to the overlaps results in higher roughness values, which in turn has been shown to promote biocompatibility [9]. An increase in the roughness leads to an increase in the overall surface area thus promoting both cellular adhesion and enhanced light absorption [53].

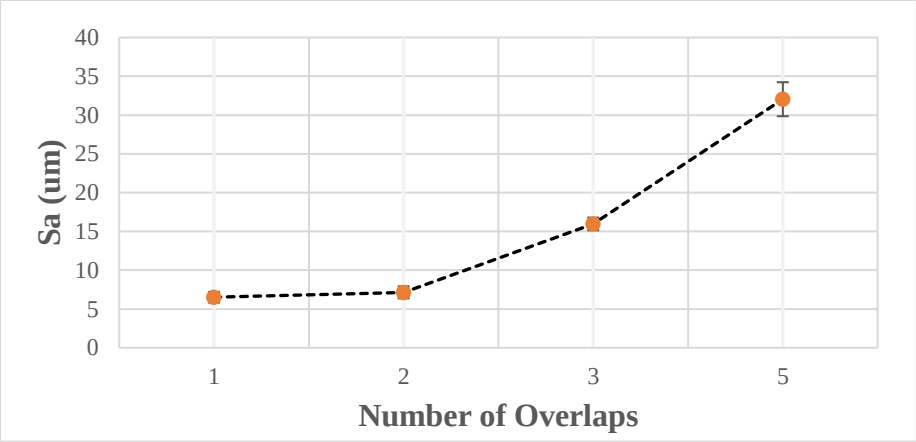

Fig. 9 Roughness measurements of Silicon samples processed at 12 W, 0.025 mm line spacing, and overlaps ranging from one to five.

4.3 Light Absorption

Light absorption coefficients were experimentally determined through light spectroscopy. As Fig. 11 shows, the closer line spacings resulted in much lower reflectivity, or higher absorption due to the closeness of each ablated line. As mentioned previously, higher overlap number increases light absorption. These measurements are also in agreement with the roughness values collected for similarly processed samples mentioned in the previous section. From these theoretical absorption values, the maximum was found in each case and used to determine a precise reflectivity coefficient for comparative purposes.

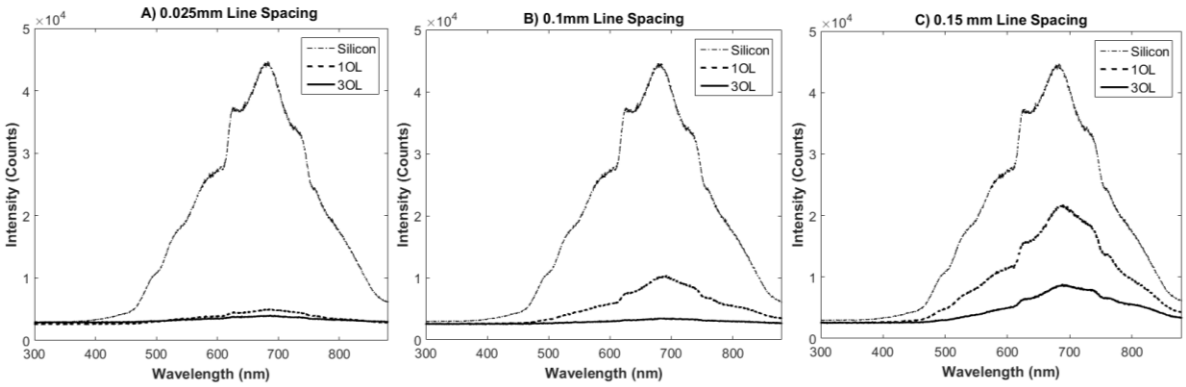

Fig. 10 Light absorption of laser treated Silicon samples at 1 and 3 OL and at line spacings of 0.025 mm, 0.10 mm, and 0.15 mm.

The effects of line spacing on reflectivity were also studied (Fig. 11). Comparing the results from one overlap, increase in line spacing resulted in a much higher reflectivity. As expected, porous and fibrous Silicon absorbed more light than Silicon showing signs of microparticles alone. At larger line spacings, portions of the Silicon were not laser ablated; instead, microparticles resting on a smoother surface remained, which exhibited reflective properties more akin to those of unprocessed Silicon. The trends were measured and were shown to exhibit a parabolic relationship, where an increase in line spacing causes a parabolic increase in the reflectivity.

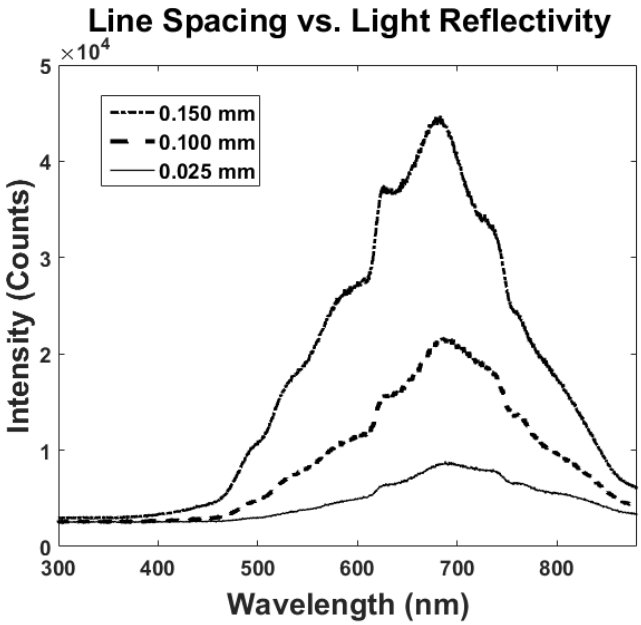

Fig. 11 Light absorption of laser treated Silicon samples at 1 OL and line spacings of 0.025 mm, 0.10 mm, and 0.15 mm.

Photon energy generally explains the theory behind absorption. Semiconductors such as Silicon have energy bands occupied by electrons which can be excited by lasers. The excited electrons can then interact and transfer energy and momentum to the lattice phonons, which are modes of vibration of the lattice. As any material, some light is absorbed and some light is reflected from the surface because of discontinuities in the real index of refraction. The fraction of the incident power reflected from the surface depends on the angle of incidence of the light, the index of refraction of the atmosphere, and the material.

Once the incident light enters the material, the absorption causes a reduction in the light intensity as the depth increases based on the material's absorption coefficient, α. Assuming a uniform material with a constant α, the intensity decay with depth z follows the Beer-

Lambert law, where I_a represents the intensity inside the surface after considering reflection losses [3, 67].

$$\boldsymbol{I(z) = I_a e^{-\alpha z}} \qquad \textbf{Eq. 39}$$

Laser ablation is highly dependent on the heat transfer to the material. With nanosecond lasers, it is generally assumed that most of the absorption is due to single photon interactions. Increases in light absorption result in higher temperatures and plume pressures [68], which encourage nanofibrous structure formation.

When the thermalization rate is greater than the laser-induced excitation rate, the process is referred to as photothermal or pyrolytic, where the absorbed laser energy is assumed directly transformed into heat. Photothermal processing leads us to the modeling of heat flow through the material. Its response to the laser is due to thermal effects in both its temporal and spatial coordinates and can be modeled from derivations of the heat equation. To mathematically determine the expected average temperature of the samples surface, the maximum temperature occurring at the end of the laser pulse is determined using Eq. 14 described in the methodology section.

The laser pulse duration in our case was of 57.5 ns, with a spot diameter 20 μm at a frequency of 100 kHz, and an average power of 12 W. The thermal diffusion coefficient - for Silicon was set at 0.000085 m^2/s, the residual energy coefficient K was set at a constant of 0.8 for Silicon, and the thermal conductivity k at 155 W/mK. R in this case is the reflectivity value experimentally determined. From this, the average surface temperature after *n* pulses was calculated according to Eq. 17 previously described. Assuming no particle evaporation, plots of the average temperatures reached by the samples for line spacings of 0.025 mm, 0.1 mm, 0.15 mm at one and three overlaps were generated as seen

in Fig. 12.

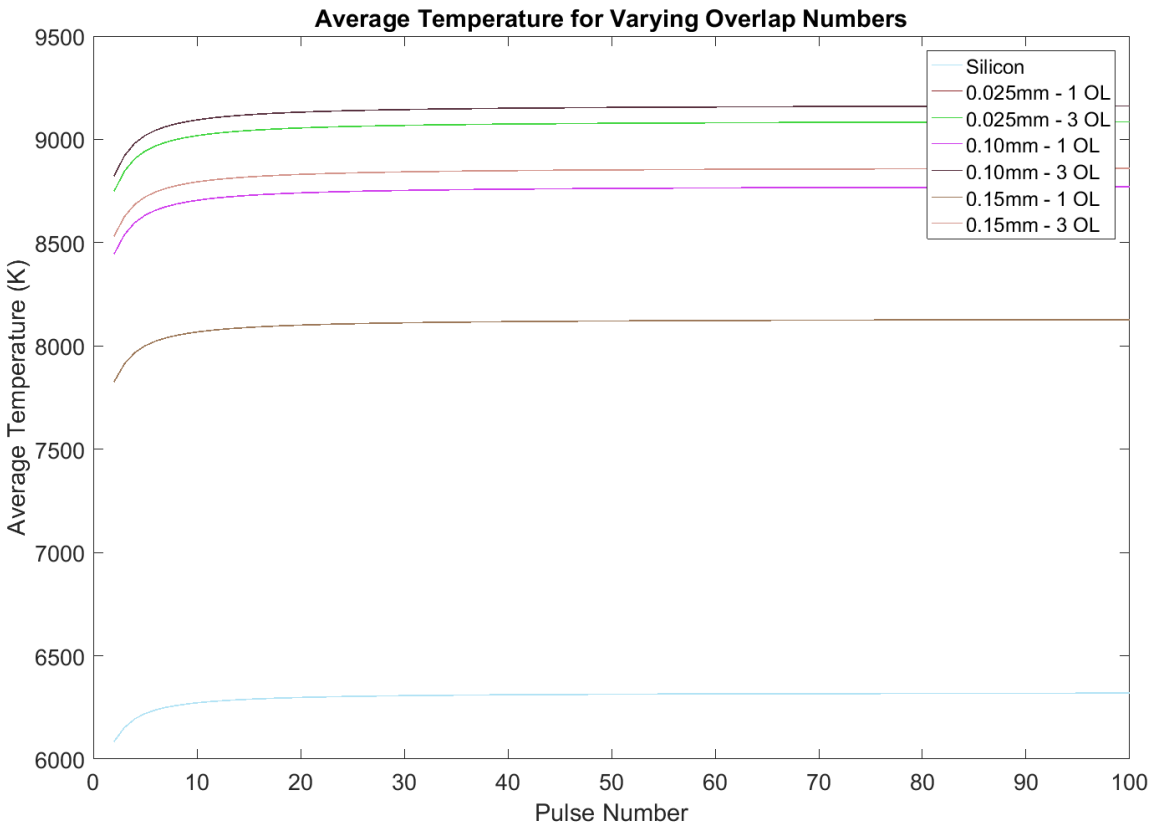

Fig. 12 Theoretical average temperatures reached by laser-ablated single crystalline Silicon samples.

From the temperature profiles shown above, there is a gradient that forms before the maximum average temperature is reached. This gradient is a result of the heating rate being larger than the cooling rate. As the pulse number increases, the cooling and heating rates approach each other causing the saturation in the temperature curves. The steady state maximum values for each of the samples was determined and as concluded, the samples at three overlaps theoretically reach a higher average surface temperature than those at one overlap. This can be explained by the increase in roughness of the surface, hence leading to higher absorptions as previously noted in Fig. 9 and Fig. 10. The only exceptions are the samples at a line spacing of 0.025 mm, where both these samples resulted in the same

maximum average temperature. This is due to the very close correlation in their reflectivity values.

The average number of particles evaporated from the surface by successive pulses was theoretically estimated based on laser processing parameters and material properties. The evaporation rate by single pulse ablation is calculated through Eq. 22.

Using its result and converting the rate into a number of atoms based on the atomic mass of Silicon, the average number of evaporated particles can be estimated as described in Eq. 23. The parameters used in this case include an equilibration time, t_{eq}, of 1.8×10^{-10} seconds, a laser frequency R_{rep} of 100 kHz, a pulse dwell time D_t calculated from the effective number of pulses, and finally a focal area A_{foc} calculated from the theoretical minimum laser spot diameter. The result was an estimated evaporation rate by single pulse ablation of $7.11145506619\times10^{17} atoms/m^2$, and the number of evaporated atoms by successive pulses was of 27 608 atoms. Values were determined for both the evaporation rate and the estimated number of evaporated particles at different laser absorption coefficients. The results are graphically shown in Fig. 13.

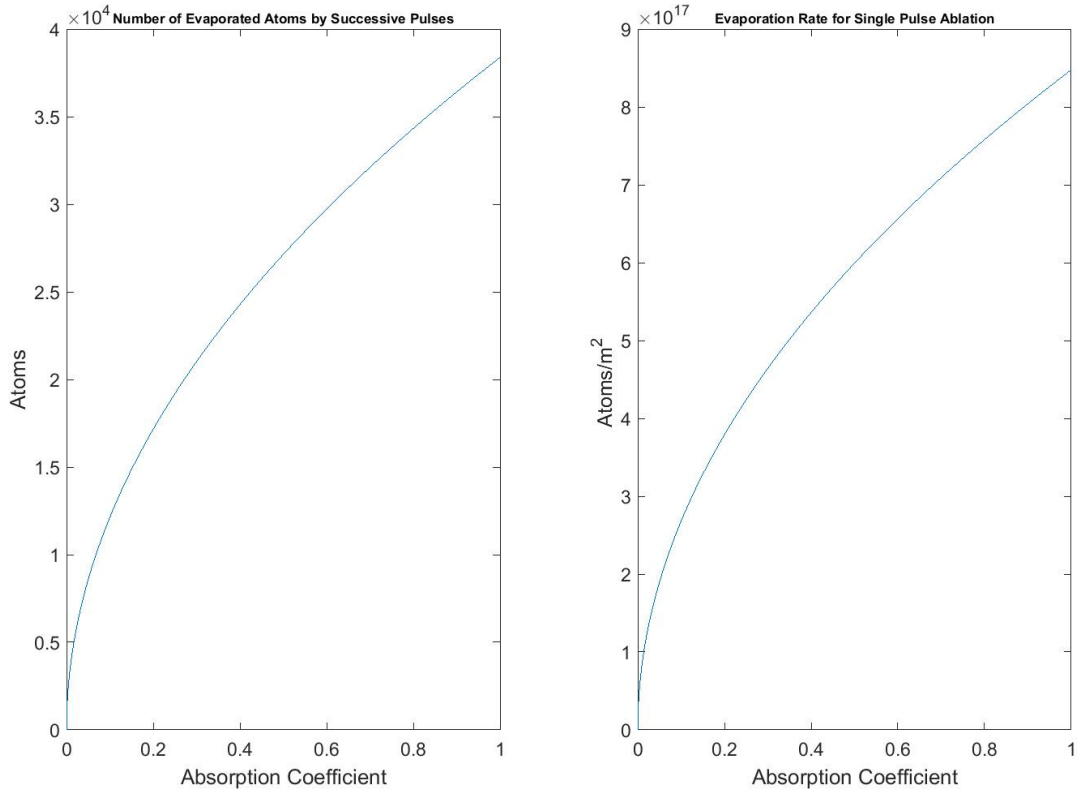

Fig. 13 Theoretical (A) number of evaporated atoms by successive pulses and (B) evaporation rate for single pulse ablation at varying absorption coefficients.

As absorption increases, the average number of atoms as well as the rate begins by increasing seemingly parabolically. There is a rapid increase in the number of evaporated atoms at lower absorption values. Although a higher number of atoms can be achieved as the absorption increases, the curve no longer grows as rapidly. This explains why Silicon laser processed surfaces with higher absorption coefficients are more likely to have nanoparticles and fiber formations as the number of evaporated atoms increases, thus allowing for more structural rearrangement.

Another theoretical factor that can be estimated is the plasma pressure and the interface thickness to which it reaches in the sample. As expected, an increase in the average power causes an increase in the estimated maximum plasma pressure as seen in Fig. 14. A higher

power results in higher energy depositions onto the surface, hence heating the material and increasing the excitation of the surface elements. The plasma pressure follows a parabolic trend, where a steeper increase in the pressure is seen at lower powers. As the plasma pressure increases, the depth affected by the latter increases linearly. The increased interface thickness allows for more of the material to be ablated and rearranged into new structures, following a similar theory to the increase in evaporated atoms previously discussed.

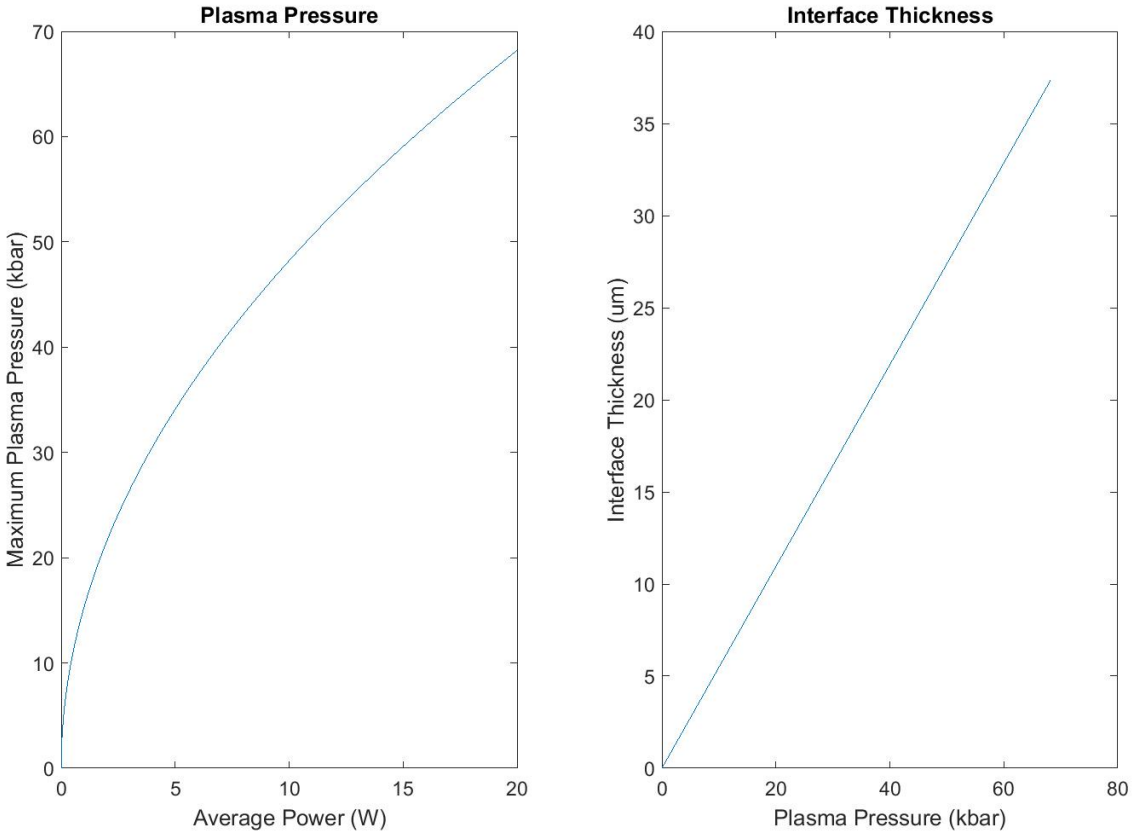

Fig. 14 Plasma pressure and interface thickness estimated at different average powers.

Chapter 5

5.0 Synthesis of Silica Nanofiber/Gold Nanoparticles Composite Induced by Laser Pulses [1]

The samples prepared at an average power of 12 W and at a line spacing of 0.025 mm were sputtered with Gold to assess their conductive properties. Samples were Gold coated for either four or eight minutes and also compared to uncoated samples. The conductivity and particle size effects were measured and compared at different overlaps.

Fig. 15 shows the EDX and TEM results of the 0.025 mm ablated Silicon samples. The Oxygen concentrations are seen to rise with increasing overlap numbers (A) to (C). The highest count for Oxygen is seen in the sample with the highest absorption, namely at five overlaps (C). As the nanofibrous generation, overall average temperature, and number of evaporated atoms of a sample increase, there are more particles interacting with the ambient air in which the ablation is being conducted. This results in particles rich in Oxygen due to the oxidation reactions occurring within the laser plume.

[1] S. Hamza, A. Ignaszak, A. Kiani (2017) "Synthesis of silica nanofiber/Gold nanoparticles composite induced by laser pulses for sensing devices fabrication" *Nanoscale Research Letters* (Submitted; under review)

S. Hamza, A. Kiani (2017) "Laser-Generated Silica Nanofibers Embedded with Electrospun Gold Nanoparticles: A Novel Platform for Biocompatible Sensing Devices" 33rd Annual Meeting of the Canadian Biomaterials Society (accepted)

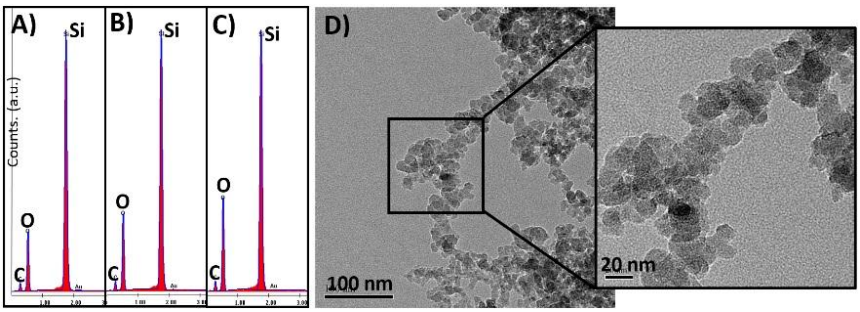

Fig. 15 TEM and EDX images of laser processed Silicon at 0.025mm. (A) 1 OL, (B) 3 OL, (C) 5 OL, (D) 5 OL.

SEM images were analyzed using ImageJ to determine the approximate diameters of the fibers occurring at the 0.025 mm line spacing. As referenced in Fig. 16, the fiber diameters grow larger as overlaps are added. From above, we know that the Oxygen levels increased with the addition of overlaps, hence partially explaining the growth in size of the fibers.

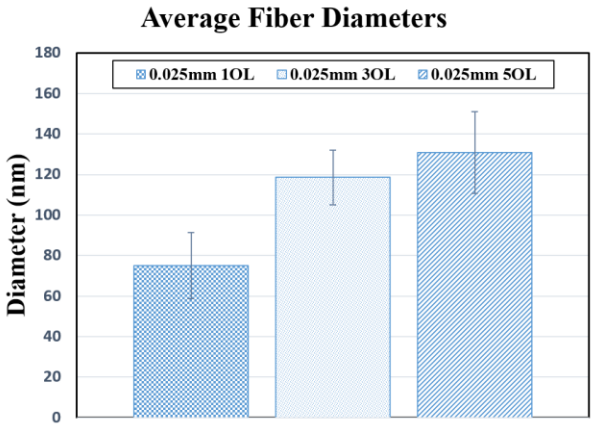

Fig. 16 Average fiber diameters calculated from SEM images at 1 OL, 3 OL, and 5OL.

Through TEM images the average Gold and Silicon particle diameters were calculated along with their standard deviations. As the number of overlaps was increased, it was found that the average Silicon particle diameter grew as well. This agrees with both the theory that particle growth occurs with increasing absorption and with the previous results showing the expansion of fiber diameters with added overlaps. The fiber diameter increase

can be explained by the growing particle sizes of the Silicon. As shown in Fig. 17, the sample with five overlaps and a line spacing of 0.025 mm has the largest Silicon particles compared to the samples at shorter line spacings. This is also the sample with the highest absorbance value compared to the other two samples. This explains the larger fiber diameters seen in sample (B) of the figure compared to sample (A). The sample shown in (C) has an absorbance coefficient that falls between those of samples (A) and (B), thus explaining its particle growth compared to that of the other two samples.

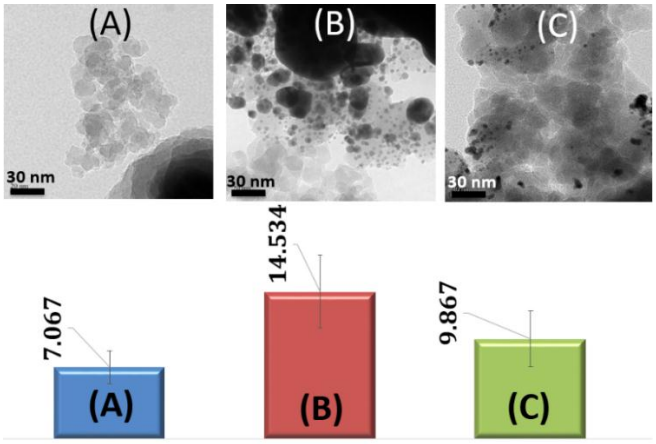

Fig. 17 Average Silicon particle diameters of samples Gold sputtered for 8 minutes. (A) 1 OL 0.025 mm, (B) 5 OL 0.025 mm, (C) 5 OL 0.15 mm.

In Fig. 18, the diameters of Gold particles are shown to have a very similar growth pattern to that of the Silicon particles. As the overlap number is increased, the Gold particle diameters are seen to increase as well. This can be explained through thin film growth patterns. The smoother surface finish and lower roughness results in more of a layer-by-layer or Frank-van der Merve growth mode [69]. As in the case for the sample at one overlap, the lowest roughness and better surface finish is seen at that sample, hence the smaller Gold particle sizes. As the roughness increases as in the sample at five overlaps and 0.025 mm, the growth is more likely to follow an Island or Vollmer-Weber mode. This

causes the particles to agglomerate or stack into small islands until the surface is covered. This explains the larger particles seen at samples with a higher roughness. Samples may also fall between the two and exhibit both forms of growth, known as the Stranski-Krastanov mode [69].

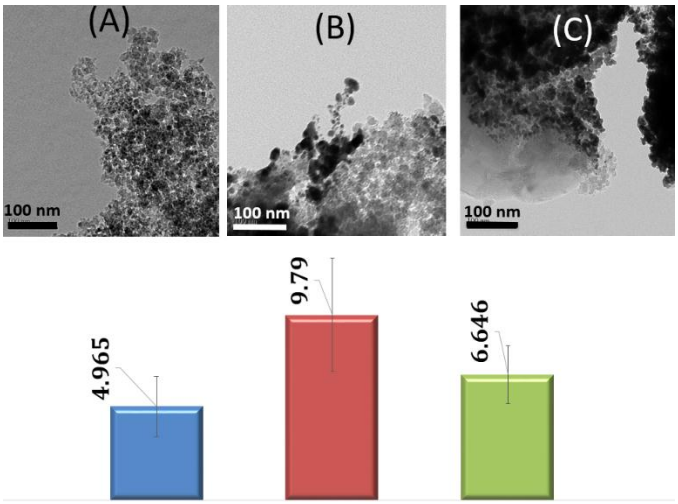

Fig. 18 Average Gold particle diameters of samples Gold sputtered for 8 minutes. (A) 1 OL 0.025mm, (B) 5 OL 0.025mm, (C) 5 OL 0.15mm.

The Gold concentration in each sample was estimated using the ImageJ software (Fig. 19) and TEM images. The concentrations were found to decrease at 0.025 mm when going from one to five overlaps. From the SEM images and fiber diameters, the Silicon sample at one overlap and 0.025 mm line spacing has thinner fibers and a smoother surface finish. As previously explained, a layer-by-layer growth mode is more likely to occur with the Gold resulting in less Gold agglomerates on the surface. At five overlaps, the fibers are much thicker and the roughness and surface finish higher, thus allowing for a less consistent thin film growth pattern. At a 0.15 mm line spacing and five overlaps, the concentration fell between that of the two previously discussed samples. When comparing the line spacings, an increase in the latter results in a decrease in Gold concentrations. The

reduction causes the absorbance of the material to decrease and hence reduces particle growth.

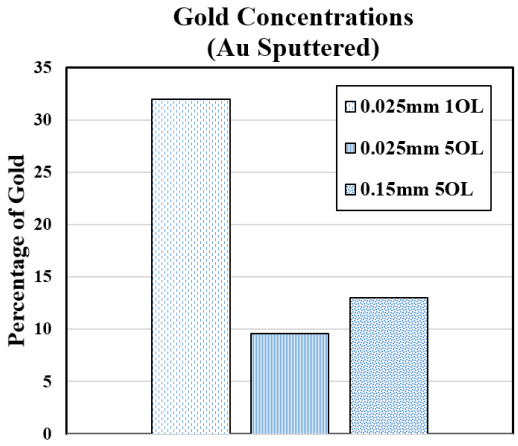

Fig. 19 Gold concentrations found on laser processed Silicon sputtered with Gold for 8 minutes at 1 OL 0.025mm, 5 OL 0.025mm, and 5 OL 0.15mm.

Theoretically, longer pulse durations and higher plume density and temperatures result in larger nanostructure formation. Nanostructure sizes depend highly on the plume diffusion time scale while their type depends on the density of the evaporated atoms. For this reason, to achieve nanofibrous structures, the laser pulses must be kept continuous for the plume density to remain at the critical level required for their formation. Hence, the larger particle sizes with growing overlaps can be explained in this fashion due to the higher overall surface temperatures and absorption coefficients [35].

5.1 Roughness

Roughness measurements were taken for samples at one and two overlaps sputtered with Gold at different durations as seen in Fig. 20. At one overlap, the surface is not nearly as rough as at two hence the close roughness measurement between no sputtering and that of four minutes (p-value: 0.148). It should also be noted that only one standard deviation was

used in these measurements. As the sputtering duration is increased, a thicker layer of Gold accumulates onto the surface, hence covering and minimizing the roughness of the processed samples. When the samples are not coated, there is a clear distinction between the roughness values, however by eight minutes of sputtering the roughness of the samples at one and two overlaps are very close in value suggesting a reduction in the biocompatibility due to the decrease in roughness [9]. This is further backed by a Tukey comparison suggesting no significant difference between the means of the samples sputtered for eight minutes.

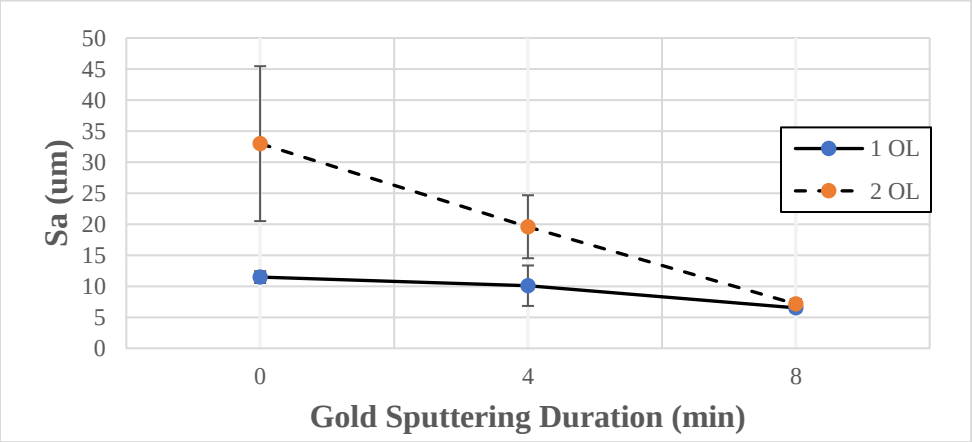

Fig. 20 Roughness measurements of samples tested at one and five overlaps at different sputtering times (0, 4, or 8 minutes).

5.1 Conductivity

The overall conductivity was measured through impedance spectroscopy for samples with one and two overlaps at a line spacing of 0.025 mm. The conductivity was measured by connecting the processed Silicon samples directly to the spectrometer. The obtained readings were resistance values at varying frequencies, which were then used to calculate the conductivity in Siemens per centimeter. This was done assuming uniform thicknesses

of the samples. Fig. 21 shows the clear distinction between overlaps and their conductivity. Since Gold is a highly conductive element, it is expected that a sample containing more of it would have an enhanced conductivity. Previous studies developing a transistor have found that Gold nanoparticles resulted in improved electrical performances [43]. The sample sputtered for eight minutes with Gold resulted in a higher conductivity than that sputtered for only four minutes. Samples with two overlaps are shown to have a lower conductivity than samples with one overlap as shown in (C). As previously denoted, the Gold concentration decreased with increasing overlaps, and the Oxygen content increases with overlaps, hence explaining the reduction in conductivity.

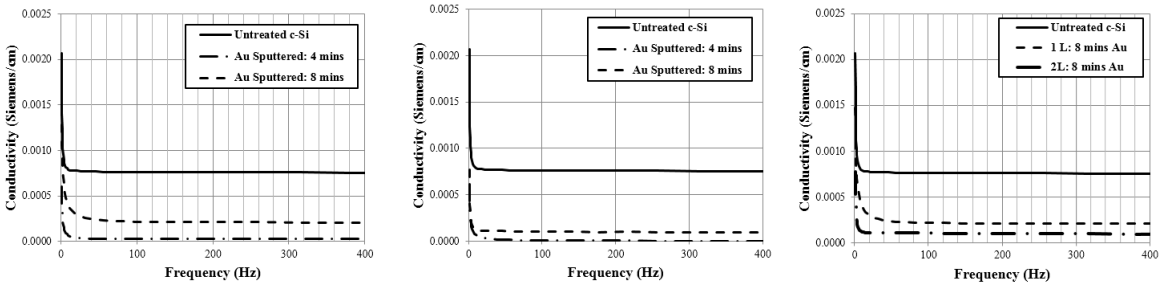

Fig. 21 Conductivity of Gold sputtered Silicon samples. (A) 1 OL, (B) 2 OL, (C) 8 minutes of Gold sputtering at 1 and 2 OL.

The conductivity measurement difference is less significant between two and three overlaps than between one and two, suggesting the approach of a threshold as seen in Fig. 22. A decrease in conductivity compared to unprocessed Silicon of approximately 10% is seen after one overlap, whereas a decrease of about 57% and 63% are seen at one and three overlaps respectively, with a p-value of 0.495 suggesting strong evidence to reject the null hypothesis.

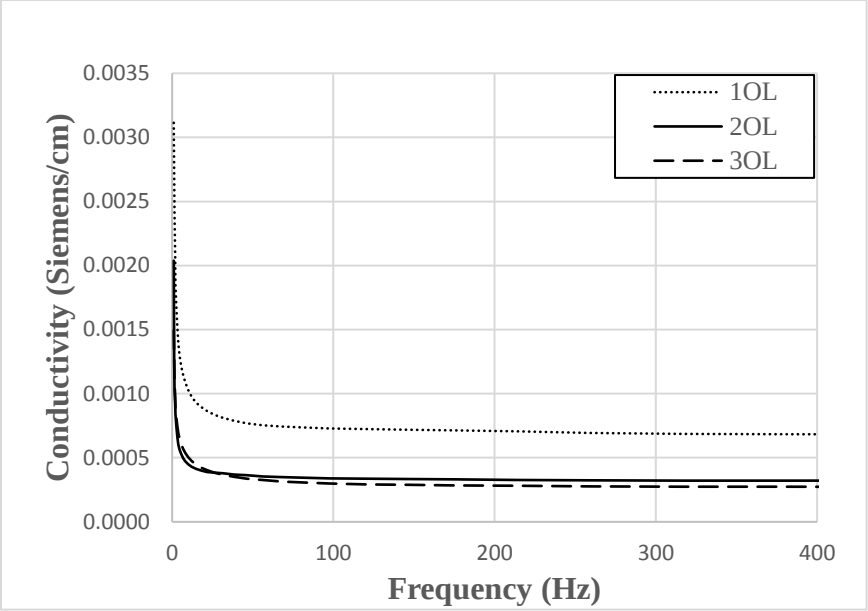

Fig. 22 Conductivity of processed Silicon samples at one, two, and three overlaps.

From Eq. 38 outlined in the methodology section, an approximate thickness of the Gold layer sputtered onto the surface can be estimated. For this experiment, the current was set at 40 mA and the voltage at 1.4 keV. This resulted in an estimated thickness of 112 nm when processed for four minutes, and 224 nm when processed for eight. Unlike the PVD thin film coated samples with a Gold layer of 1000 nm, the coating thickness of these is nearly a tenth their value. One can easily expect to see higher conductivities in the thin film samples than in the latter. As seen in Fig. 23, a clear distinction between the duration of the Gold coatings can be made. This also enables us to conclude a certain amount of controllability in the conductivity of the samples.

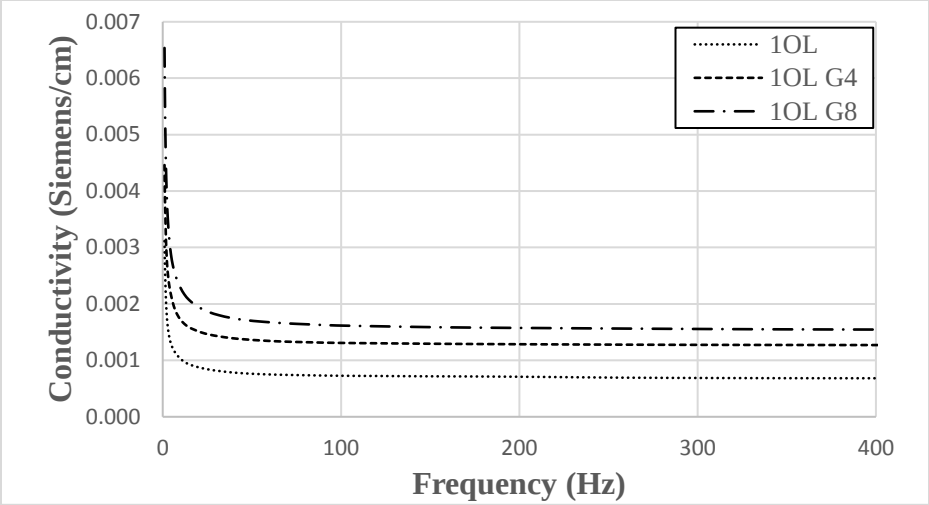

Fig. 23 Conductivity of Gold sputtered Silicon samples at one overlap with a sputtering duration of zero, four, or eight minutes.

Samples processed at two and three overlaps exhibited similar features as seen in Fig. 24, where a higher sputtering time resulted in a higher conductivity. As previously mentioned in the literature review, a higher concentration of conductive particles results in a higher overall conductivity of the insulating material [61].

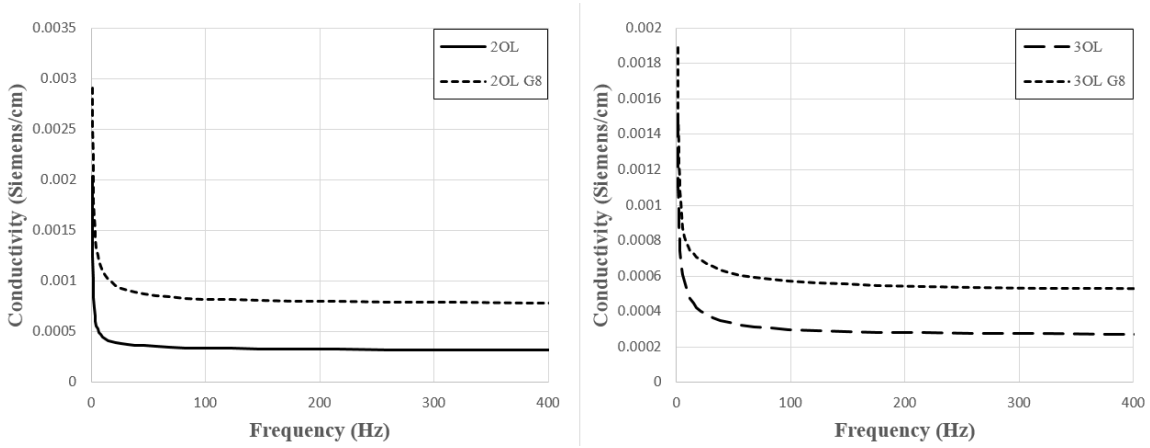

Fig. 24 Conductivity of processed Silicon samples at two and three overlaps with either no Gold or Gold sputtered for eight minutes.

As discussed in section 2.4, the conductivity of Silicon dioxide is dependent on the distance between the conductive particles according to the theoretical model. Higher numbers and larger particle radii of Gold nanoparticles result in a higher volume fraction, which in turn results in increases in interparticle distances. From the measured particle sizes depicted earlier in Fig. 18, the relationship between the Gold particle radii and the conductivity agree with the theoretically proposed relationships. The greater the distance between the conductive Gold particles, the lower the overall conductivity of the silica. As seen in Fig. 25, the Gold particle distances increase with a decrease in overlap, further agreeing with the conductivity measurements expected.

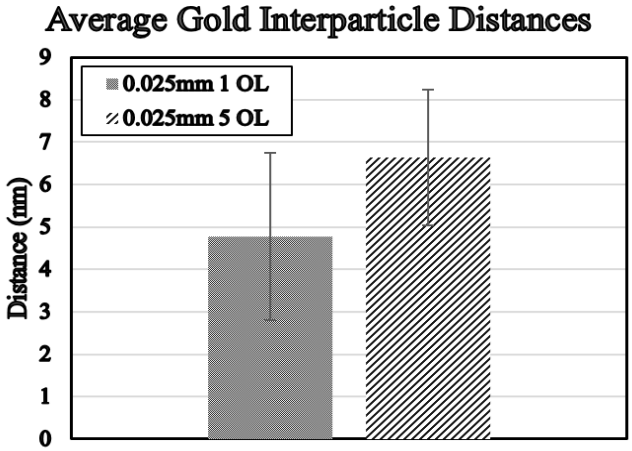

Fig. 25 Experimental interparticle distances of Gold sputtered Silicon samples. (A) 1 OL, (B) 5 OL.

5.2 Biocompatibility

This section aimed to investigate the potential biocompatibility of the a treated sample using a solution of SBF. As seen in Fig. 26, the black outline depicts the results of an untreated sample having been submerged in the solution. No traces of Calcium, Oxygen, or Phosphorous can be found from the results, which are key elements in the beginning of

the formation of hydroxyappetite on the surface [27]. The red curve seen in the image below represents a sample that was laser processed, which shows results of potential hydroxyappetite formation due increases in the traces of elements such as Calcium and Phosphorous on the surface post analysis. This suggests biocompatibility of the processed samples, however conclusive results cannot be drawn without further in-vitro testing. Cellular interactions with the sputtered substrate should be further examined with a variety of different cells. On the long-term, in-vivo tests should be conducted to ensure viability.

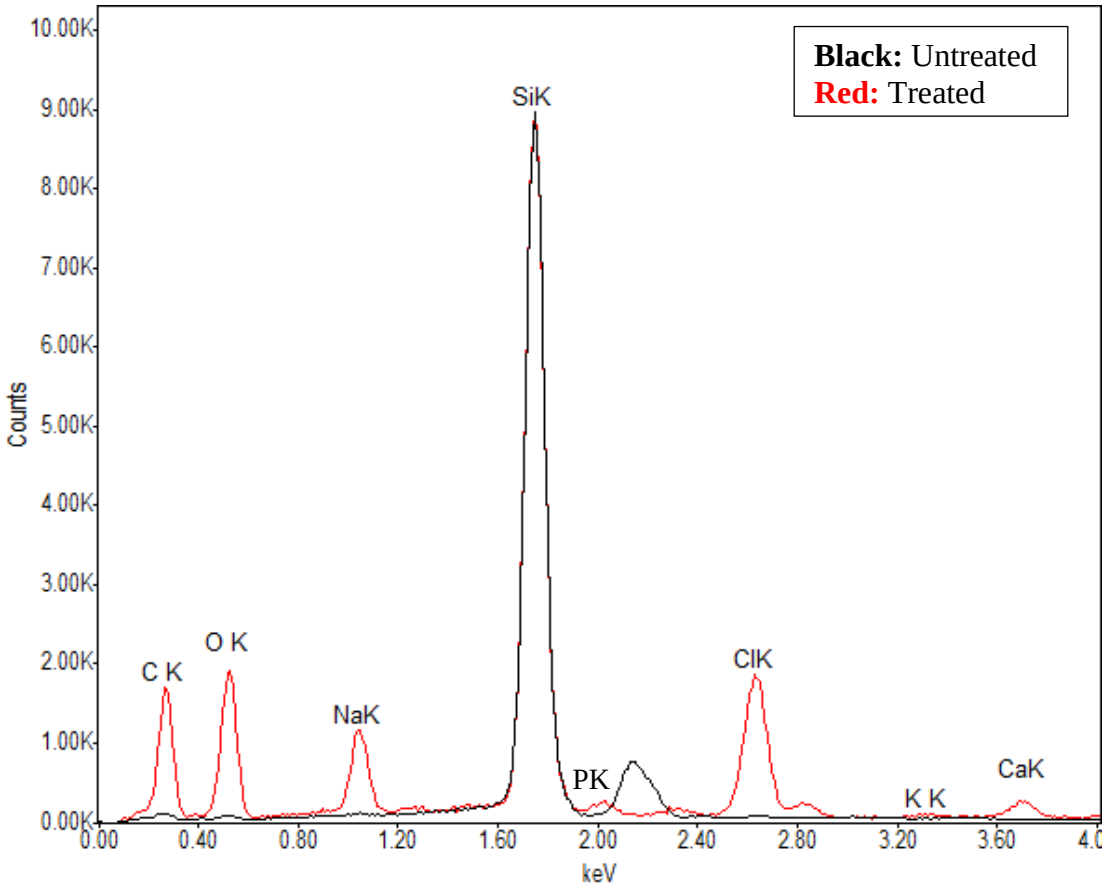

Fig. 26 EDX results of untreated and laser treated samples.

Chapter 6

6.0 Silica/Gold Hybrid Nanofibers Induced by Laser Processing of Silicon Coated by Gold Thin-Film [2]

Samples were prepared on an evaporated Gold wafer at average powers of 2.35 W, 4 W, 9 W, and 12 W. The line spacing was originally kept at 0.01 mm and 0.025 mm for these samples, however due to the results obtained at the higher powers of both 9 and 12 W a larger line spacing of 0.05mm was used to process the mentioned samples. The overlaps were varied at either one, three, or five and the conductivity and particle size effects were measured and compared at the different powers and overlaps. As previously mentioned, Gold sputtering is a controlled method, allowing us to regulate the Gold concentrations, and overall conductivity. The purpose of conducting the same experiment on the thin film is to compare the efficacy of both methods and suggest future advances.

The TEM images were first analyzed to determine the changes in Gold concentrations and particle sizes of both Silicon and Gold (dark spots). It is clearly observed that as the overlap number is increased, the Gold particles become sparser, having evaporated into the

[2] S. Hamza, A. Kiani (2017) "Silica/Gold Hybrid Nanofibers Induced by Laser Processing of Silicon Coated by Gold Thin-Film for Biomedical Sensing Applications" *Sensors and Actuators A: Physical*. (Submitted; under review)

S. Hamza, A. Kiani (2017) "A Rapid and Easy Procedure of Biosensor Fabrication by Nanosecond Laser Processing of Si Wafer Coated by Gold Thin-film" 5th International Conference on Bio-Sensing Technology (accepted)

atmosphere due to the induced increased surface temperature. It can also be noted that the amount of Gold particles also decreases with increasing laser power. At 9 W and five overlaps for example, no Gold particles can be seen in the sample as denoted in Fig. 27 (F).

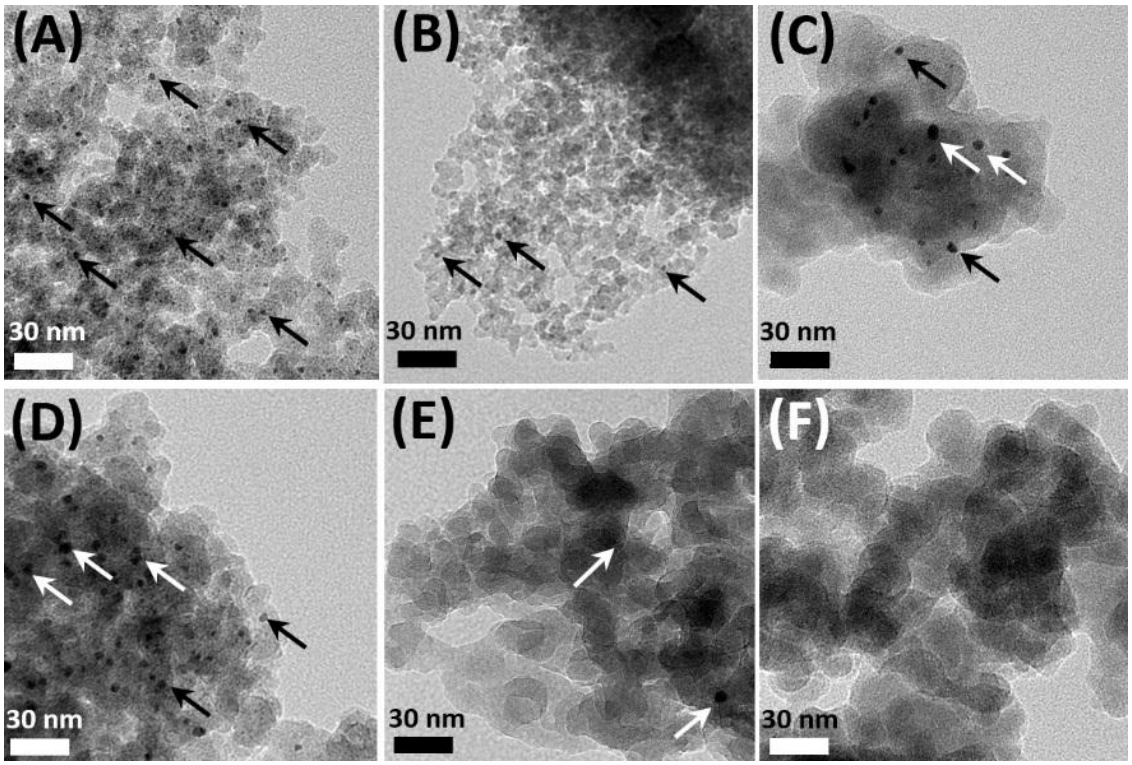

Fig. 27 TEM images of laser processed evaporated Gold Silicon wafer at 0.025mm line spacing and at different overlaps and average power: (A) 1 OL 2.35 W, (B)1 OL 4 W, (C) 1 OL 9 W, (D) 5 OL 2.35 W, (E) 5 OL 4 W, (F)5 OL 9 W.

Overall, the average Silicon particle diameters are shown to increase with the overlap number and power in agreement with the theoretical predictions previously discussed in section 2.4. At 2.35 W and five overlaps, the longest average Silicon particle diameters were measured as shown in Fig. 28 (A).

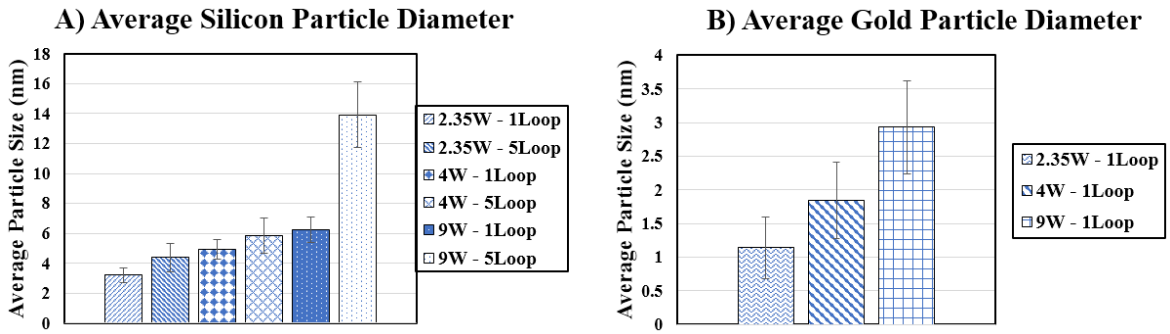

Fig. 28 Average Silicon and Gold particle diameters for thin film samples.

As the power of the processed samples increased, Gold particle growth was noted, as seen in Fig. 28 (B). Compared to the average Silicon particle size, it can be clearly seen that the Gold particles are much smaller. It should also be noted that at 9 W and five overlaps Gold particles could not be seen and hence measured. This was further ensured through EDX results, which showed little to no traces of Gold for this sample even when compared to one overlap as seen in Fig. 29.

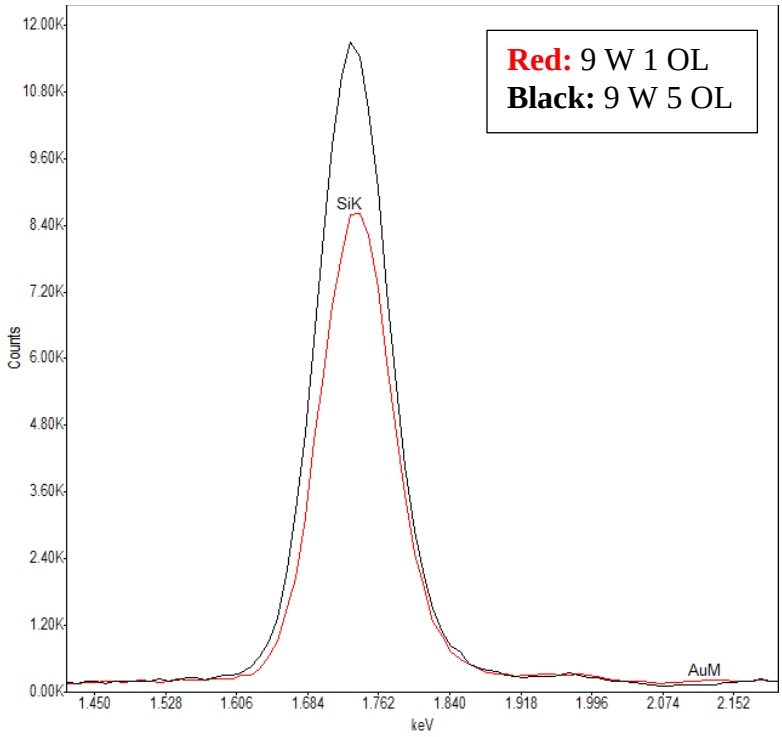

Fig. 29 EDX results comparing samples at 9 W processed at one and five overlaps.

At 2.35 W, the change in Gold concentration with increasing overlaps was of a 1% decrease, while at higher powers, the reduction was slightly more significant. As the power increases, the concentrations decreased due to a rise in the evaporation rate of the Gold particles as can be seen in Fig. 30. When the power reached 9 W and five overlaps, the overall temperature of the ablated regions and excitation of the Gold particles were too high for it to be redeposited once cooled, hence the reason none were seen in this sample.

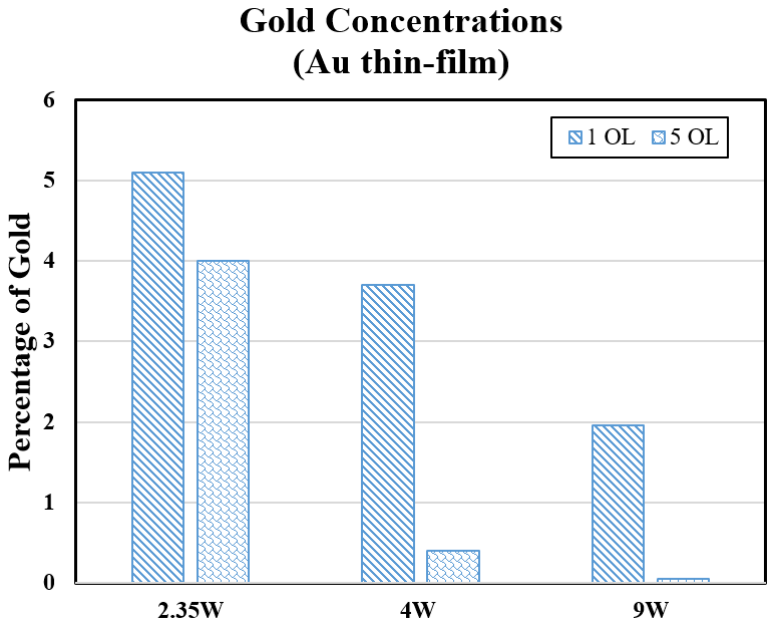

Fig. 30 Gold concentrations found on laser processed Gold coated at 0.025 mm line spacing and 1 OL and 5OL.

Images obtained from the FESEM at 2.35W and a line spacing of 0.025mm clearly show the effects of overlaps. Fig. 31 (A) shows the sample processed at one overlap. The regions ablated by the laser pulses are clearly visible in this sample, where micropores are created on the surface at each laser pulse. At three overlaps, the material is further ablated and the pores filled with the newly melted Gold, Oxygen, and Silicon material present as seen in the EDX results of Fig. 32. By five overlaps, the pores are lessened and the overall surface much smoother. Since the melting point of the surface is decreased once processed, the

increase in overlaps results in more material melting spreading over the surface. At 2.35W, the laser energy is low and does not ablate the region as strongly, hence the clear distinction of the spaces between the lines. The material at this low power distinctly outlines the appearance of the laser pulses, but no fibrous structures were seen.

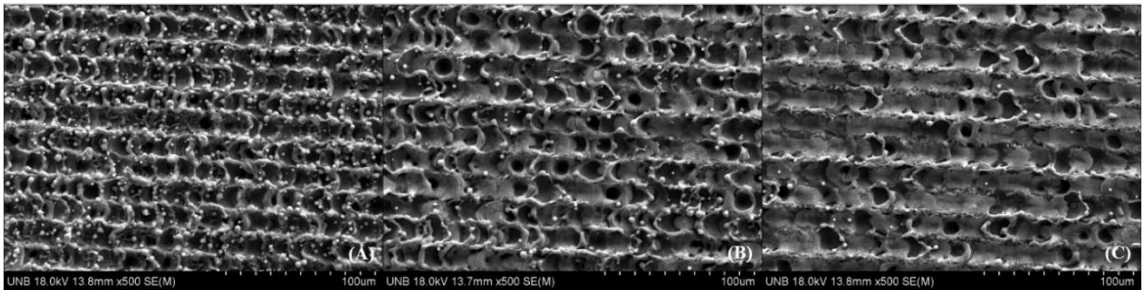

Fig. 31 FESEM images of processed Gold coated Silicon at 2.35 W and 0.025mm line spacing. (A) 1 OL, (B) 3 OL, (C) 5 OL.

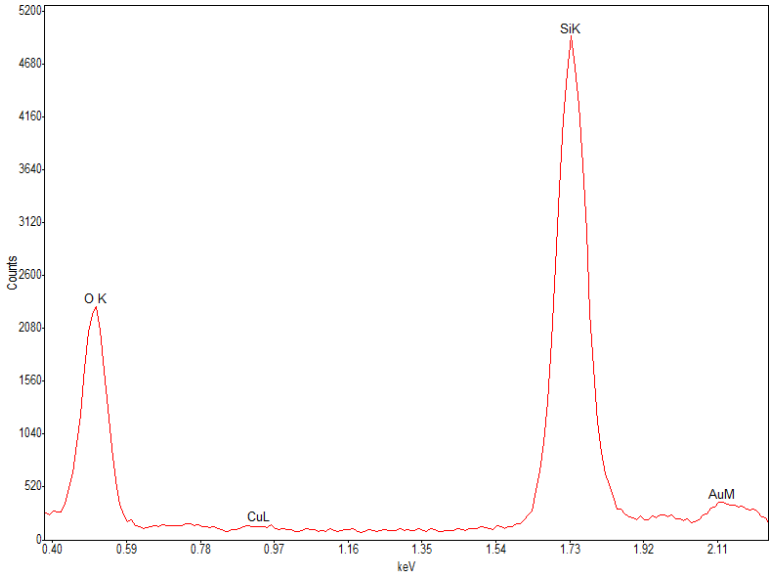

Fig. 32 EDX results for sample treated at 2.35 W showing traces of Oxygen, Silicon, and Gold.

At 4 W and a line spacing of 0.01 mm, fibrous structures were observed. Although still a low power, the shorter line spacing resulted in plume temperatures that are high enough to allow the formation of the latter. Similarly to the fibers seen in the pure Silicon samples, the fiber diameters and densities increase with increasing overlaps as previously shown in

Fig. 16. At a lower magnification, porous holes and structures have formed on the surface. Collected backscattered electrons from the FESEM result in the lighter element backscattering the electrons more strongly than the heavier element, leading to a higher contrast image. It is highly dependent on the atomic number of the element, where the higher the latter the lighter the area [70]. The FESEM scattering and backscattering images outlined in Fig. 33 clearly depict the effects of power on the samples. The darker regions represent the Silicon, while lighter areas denote the Gold. As the overlap increases from one to five, the Gold concentration can be seen to decrease through the images from (D) to (F), where the lighter areas are seen to lessen, especially when comparing three and five overlaps.

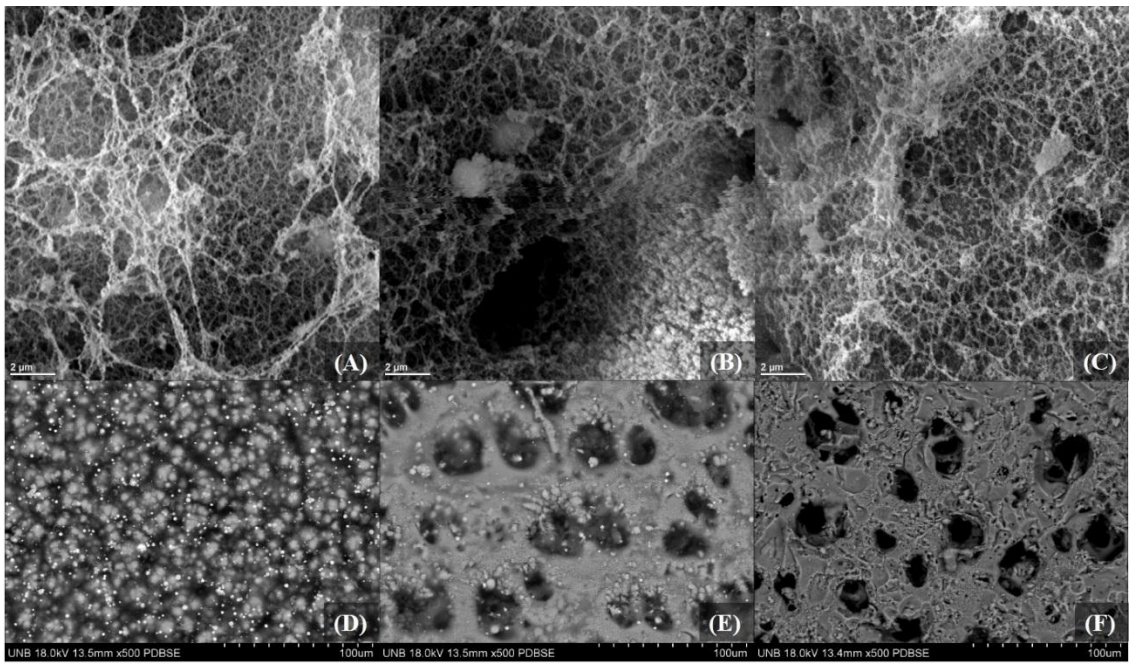

Fig. 33 Processed Gold coated Silicon at 4W and 0.01 mm line spacing. SEM images: (A) 1 OL, (B) 3 OL, (C) 5 OL. Scale: 2 **µm**. FESEM backscattering images: (D) 1 OL, (E) 3 OL, (F) 5 OL.

At a higher line spacing of 0.025 mm, fibrous structures are less clearly formed with instead the appearance of micro- and macro-porous structures. At one overlap (Fig. 34 (A)), the

porosity of the particles is not apparent at all. By three overlaps (B), the formation of spongy structures begins to appear, and by five overlaps (C) fibrous structures can be observed. Comparing the backscattering images, the highest Gold content observed is at the lower overlap, as expected. The distance between the lines is blurred as the overlap increases due to the increase in the material being ablated.

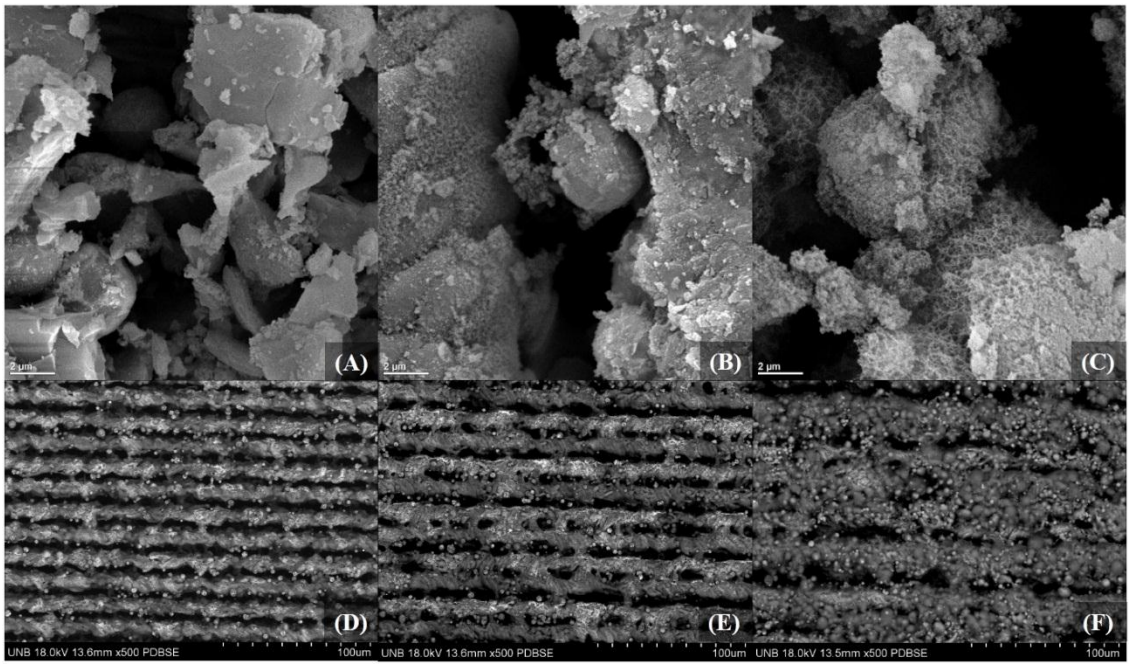

Fig. 34 Processed Gold coated Silicon at 4W and 0.025 mm line spacing. SEM images: (A) 1 OL, (B) 3 OL, (C) 5 OL. Scale: 2 **µm**. FESEM backscattering images: (D) 1 OL, (E) 3 OL, (F) 5 OL.

As the power is increased, the formation of larger particles can be seen. At 9W, the space between the ablated regions is less noticeable as the heat affected zone increases and results in a deeper groove formation with more material being evaporated and redeposited with cooling [27]. Since Gold has a lower boiling and melting point than Silicon, it is expected that it would evaporate at higher powers due to the increase in plume temperature.

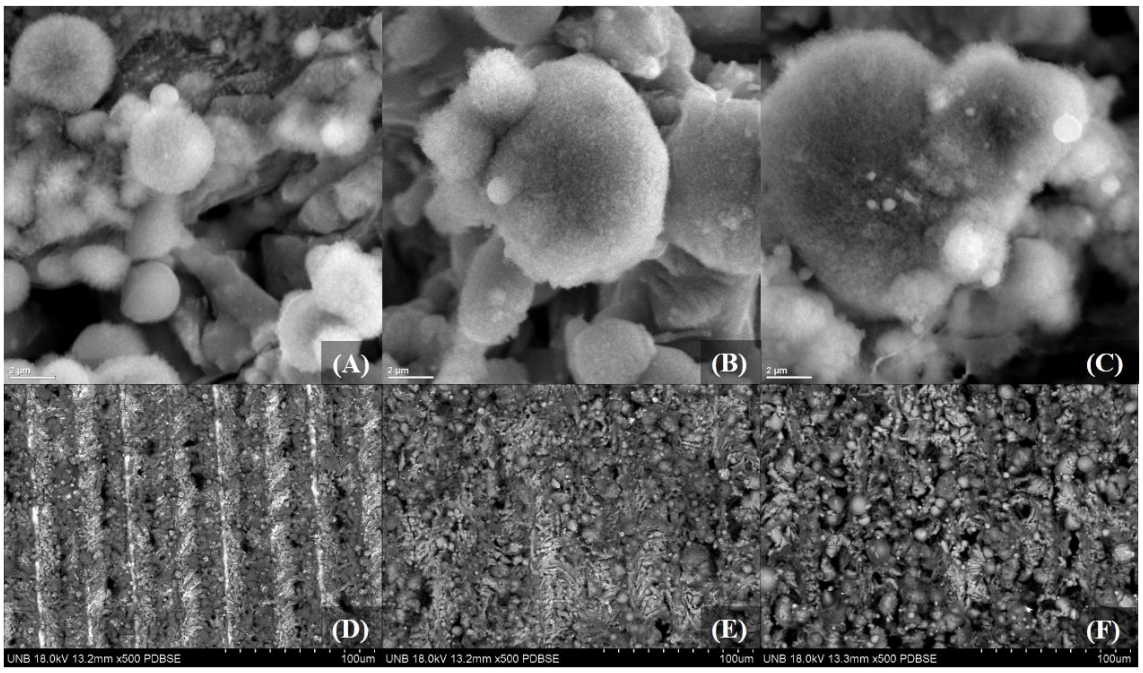

Fig. 35. Processed Gold coated Silicon at 9W and 0.05 mm line spacing. SEM images: (A) 1 OL, (B) 3 OL, (C) 5 OL. Scale: 2 **µm**. FESEM backscattering images: (D) 1 OL, (E) 3 OL, (F) 5 OL.

For the samples processed at the higher powers of 9 W and 12 W, a larger line spacing was chosen to minimize the Gold evaporation from the surface. Samples were processed at both 0.025 mm and at 0.05 mm and imaged for comparison. Fig. 35 denotes the samples processed at 9 W and at 0.05 mm. Porous and spongy structures have clearly formed at all overlaps, with their growth increasing with the latter and as previously discussed. As seen at both 2.35 W and 4 W, the overlap causes a decrease in the appearance of the lines and the Gold concentration, with larger porous structures occurring as well. A magnification of these images under the FESEM using backscattering electrons allows us to clearly see the different shapes and effects made by the processed Gold. Samples at 0.025 mm on the other hand showed fibrous structures occurring at three and five overlaps as seen in Fig. 36 (B) and (C), however only microporous structures at one overlap were detected.

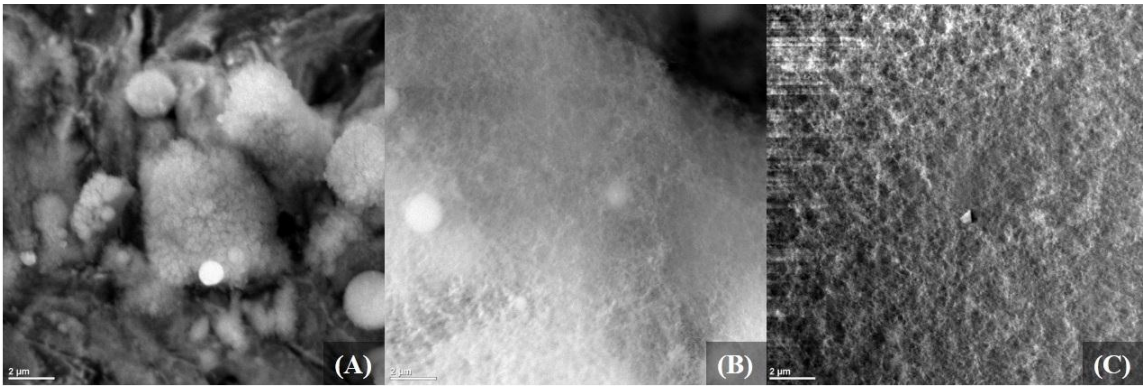

Fig. 36 FESEM images of processed Gold coated Silicon at 9W and 0.025 mm line spacing. (A) 1 OL, (B) 3 OL, (C) 5 OL. Scale: 2 **µm**.

Observing these samples using backscattering electrons has shown some traces of Gold on the surface as shown in Fig. 37, meaning it was not all evaporated at one overlap and at 9 W. Clearly, thread or fiber-like structures of Gold can be seen on the surface of the microparticles shown in image (D). The same was observed at one overlap at a power of 4 W, shown in Fig. 37 (A) and (C). At 4 W however, a higher concentration of Gold is visible further backing our previous results regarding Gold concentration.

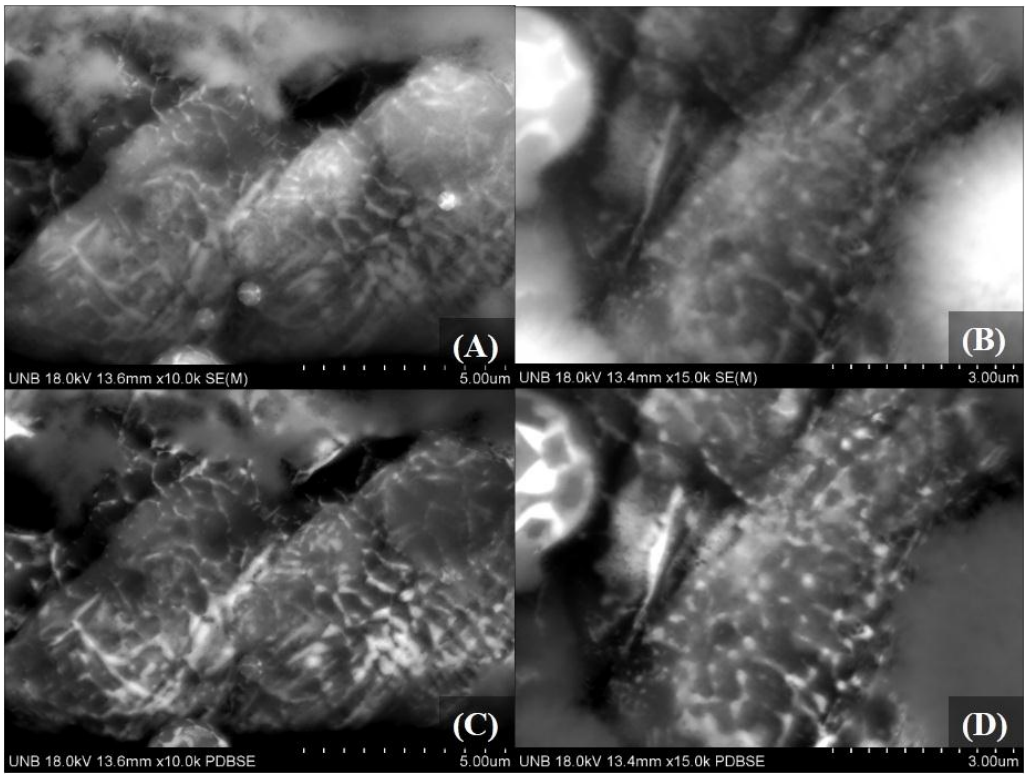

Fig. 37 FESEM images of processed Gold coated Silicon at a line spacing of 0.025 mm and one overlap. FESEM images: (A) 4 W, (B) 9 W. FESEM backscattering images: (C) 4 W, (D) 9 W.

The last samples were processed at 12 W and at a line spacing of 0.05 mm and 0.025 mm. As previously seen in the TEM images, by 9 W and five overlaps, there were little to no Gold particles left. The high power caused the Gold layer to be fully removed, which in turn one would expect to see the most fiber formation due to the increased surface temperatures expected. At one overlap for both line spacing samples (Fig. 38 (A) and (D)) however, porous spongy microstructures are seen, but not the smooth fibrous surface finish seen in the pure Silicon samples. Due to the thin layer of Gold coating the Silicon, more heat is required to achieve the threshold required to form a smooth surface of fibrous structures, hence the reason why at five overlaps the surface finish approaches that seen at one overlap in the Silicon samples processed at 0.025 mm due to the higher surface temperatures reached.

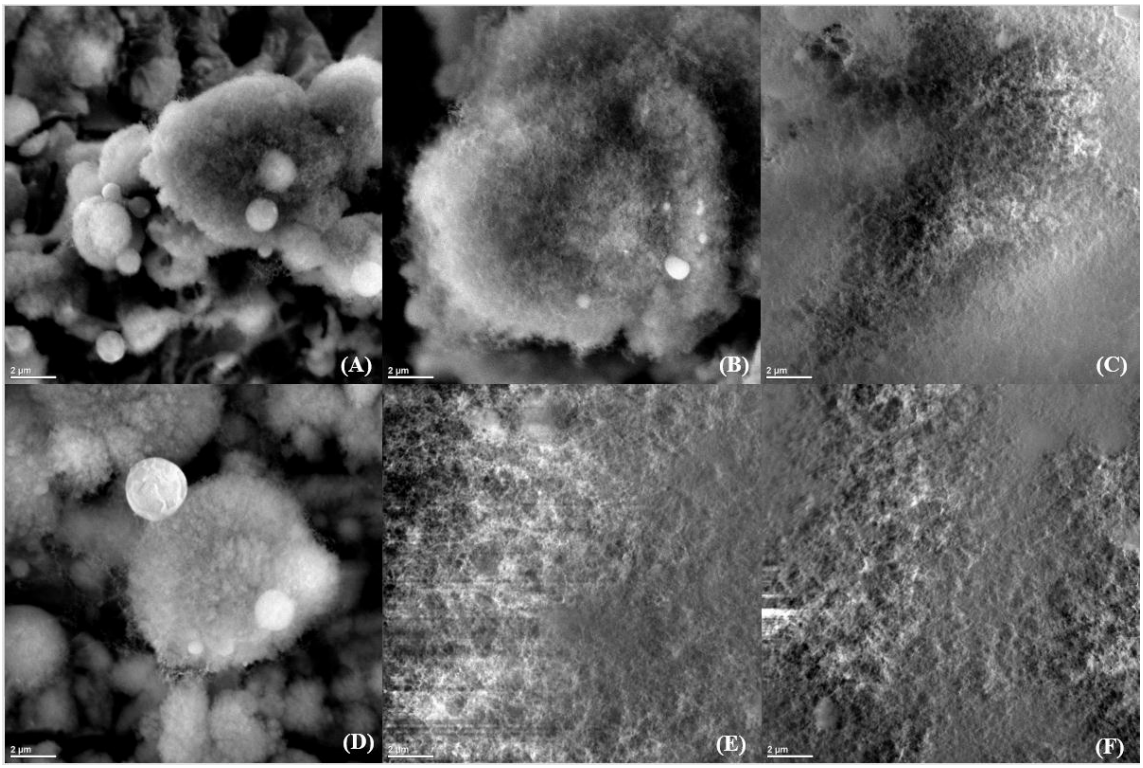

Fig. 38 SEM images of processed Gold coated Silicon at 12 W. (A) 0.025 mm, 1 OL, (B) 0.025 mm, 3 OL, (C) 0.025 mm, 5 OL, (D) 0.01 mm, 1 OL, (E) 0.01 mm, 3 OL, (F) 0.01 mm, 5 OL. Scale: 2 **µm**.

It should also be noted that all processed samples showed an increase in their Oxygen content with increasing overlaps. As seen in Fig. 39, at a line spacing of 0.025 mm and a power of 4 W, the increase in overlaps from one to five causes a distinguishable increase in the Oxygen count obtained through EDX. This will once more play a key role in the conductivity of the samples due to the insulating properties of Silicon dioxide.

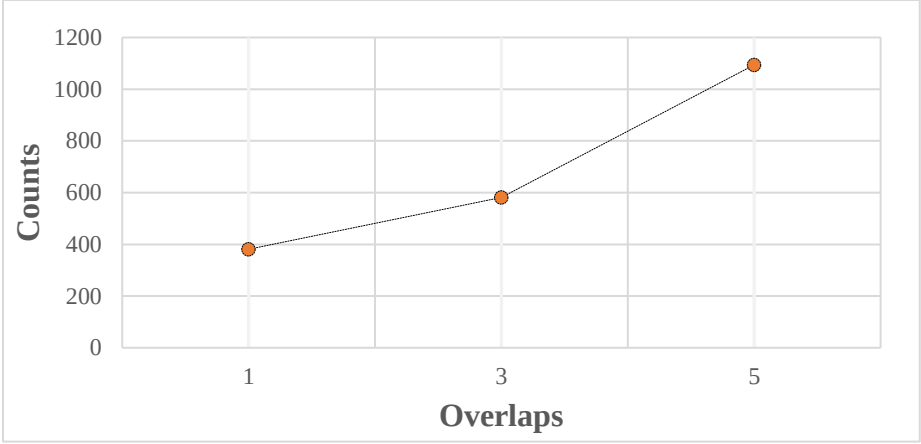

Fig. 39 Plotted EDX results for Oxygen content of thin film samples processed at 0.025mm and 4 W.

6.1 Roughness

Roughness of these samples show an overall expected trend with increasing power and overlap as depicted in Fig. 40. At one overlap, the power does not have as big an effect on the roughness of the samples where a significant increase is not observed until the 12 W power is reached. There is little evidence of a difference in the measured roughness between the 4 W and 9 W sample (p-value: 0.07). The 12 W processed sample at five overlaps has a large standard deviation, which can be attributed to only one being measured. The thin film samples are thicker than the pure Silicon wafers suggesting that higher temperatures are necessary to allow fibrous structures to form. As the overlap is increased to five, the roughness increases much more drastically. At 2.35 W, however, the power is low enough so as not to affect the roughness to the same extent as those processed at higher powers, as further seen in the FESEM images collected and previously discussed.

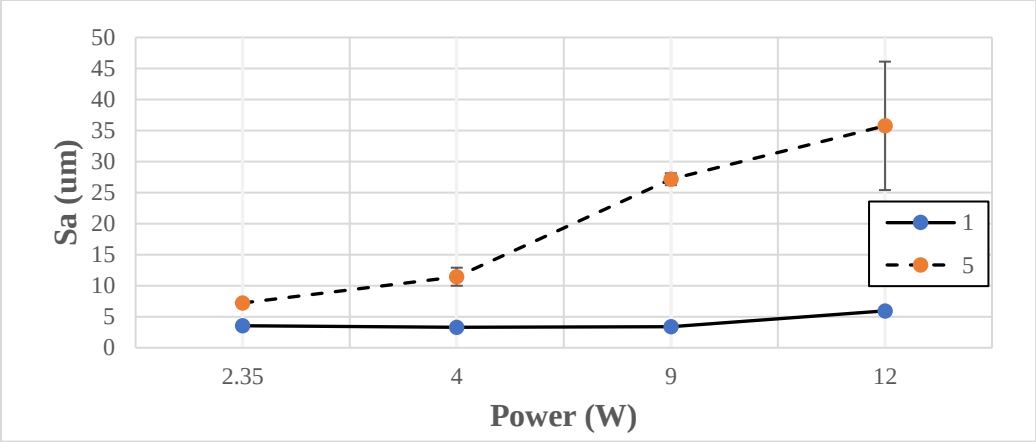

Fig. 40 Roughness values for Gold coated samples at one and five overlaps and different powers.

6.2 Conductivity

The thin film unprocessed Silicon sample has a much higher conductivity compared to that of the processed samples. As expected, the untouched Gold layer offers a path of least resistance for the current to pass through. Once the sample is processed, an increase in power results in a decrease in conductivity as seen in Fig. 41. Out of all the processed samples, the one processed at 2.35 W had the highest conductivity. This can be related to the fact that the low power caused the least ablation on the surface. At higher powers, the Gold layer was vaporized and an increase in the formation of Silicon dioxide occurs, hence the reduction in conductivity. The overlap number also reduces the conductivity of the samples. Increasing the overlap causes more material to be ablated from the surface and hence a reduction in the thin film, with the exception of the sample processed at 2.35 W as seen below.

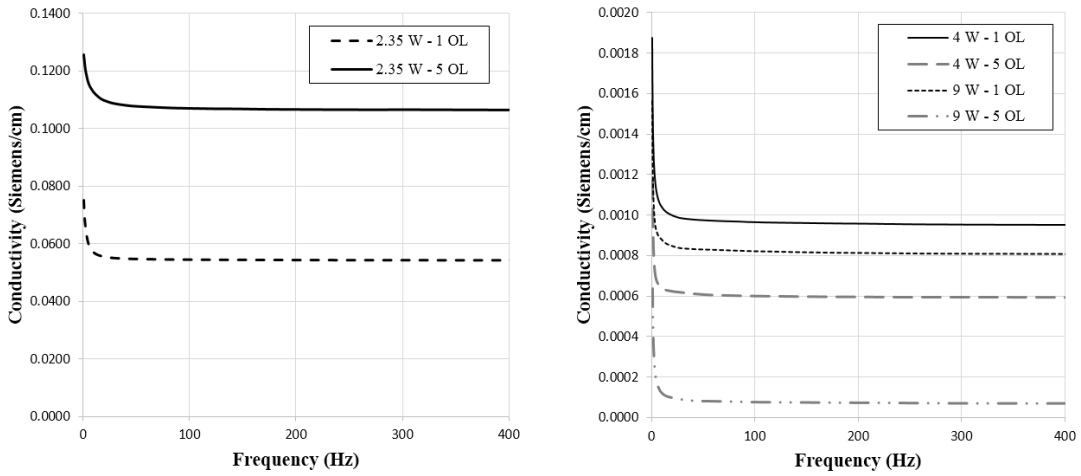

Fig. 41 Conductivity of thin film processed samples at (A) 2.35W at 1 and 5 OL, (B) 4W and 9W at 1 and 5 OL.

The distance between the Gold particles was measured from TEM images for the two samples. The Gold particles at one overlap are only slightly closer together than the ones at five as denoted in Fig. 42 below. The p-value between the latter is at 0.68, suggesting no difference between the means of the two values. This distance is in the order of a few nanometers, hence assuming the occurrence of quantum effects as discussed in section 2.4. With the Gold particles closer together, the electrons are more easily able to cross the low conductivity barrier of the processed Silicon to get to the next more conductive Gold particle [71]. It is also important to note that the size of the Gold particles plays a key role in the conductive effects of the samples. As seen in Fig. 41, the conductivity at five overlaps is higher than that at one. The size of the Gold particles is larger at five overlaps as previously seen from the collected measurements in Fig. 28, and the interparticle distance is similar to that of the sample only processed with one. This explains the shift in the expected trend of conductivity. As the overlap number is increased and the Gold particles are further dispersed, one is less likely to expect to see the quantum effects even though the Gold concentration is slightly higher. This can be related through the governing

equations of conductivity at the nanoscale level (Eq. 34 – Eq. 37). The conductivity of the insulating Silicon dioxide particles is dependent on the interparticle distance, l, of the conductive Gold particles as denoted in Eq. 36 in section 2.4 [61]. The effect on the conductivity of the Silicon dioxide then becomes highly dependent on the distance between the conductive particles. The Gold particle distances were measured, and are shown in Fig. 42 to increase with a decrease in overlap, further agreeing with the conductivity measurements expected. The greater the distance between the conductive Gold particles, the lower the overall conductivity of the silica. The distance between particles at 4 W and five overlaps and that between 9 W and one overlap show a lack of statistical significance between the means with a p-value of 0.178. This is not alarming since both these samples reach much higher temperatures and are likely to result in similar surface topographies as seen from the SEM images presented in the previous section.

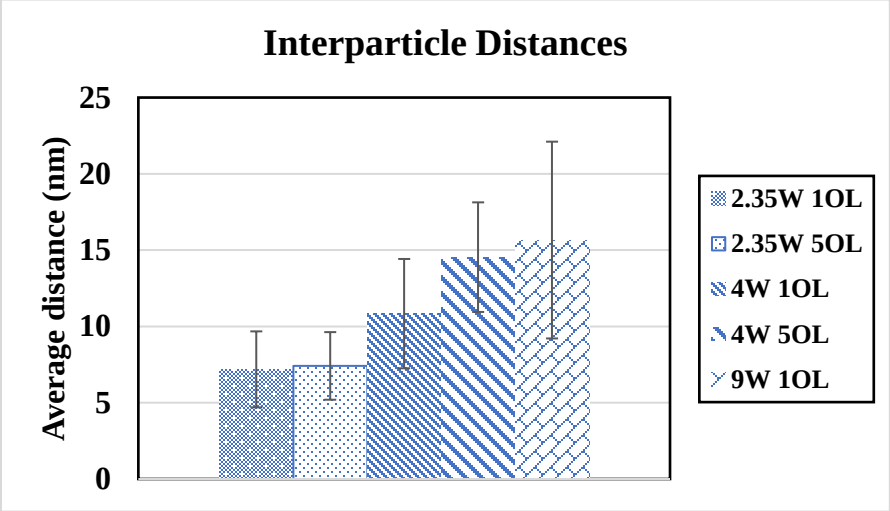

Fig. 42 Conductivity of thin film processed samples at (A) 2.35W at 1 and 5 OL, (B) 4W and 9W at 1 and 5 OL.

A spiral line pattern was also tested to ensure that conductivity was not directional. This was ablated onto the surface of the thin film samples at powers of 2.35 W and 4 W, with

all other parameters held constant. The conductivity showed similar trends to those seen in samples processed with a continuous line pattern. The 2.35 W processed samples had distinctly higher conductivity values than those processed at 4 W as seen in Fig. 43 below. As previously mentioned, this is expected due to the increasing power causing higher overall surface temperatures and hence resulting in the evaporation of the thin film.

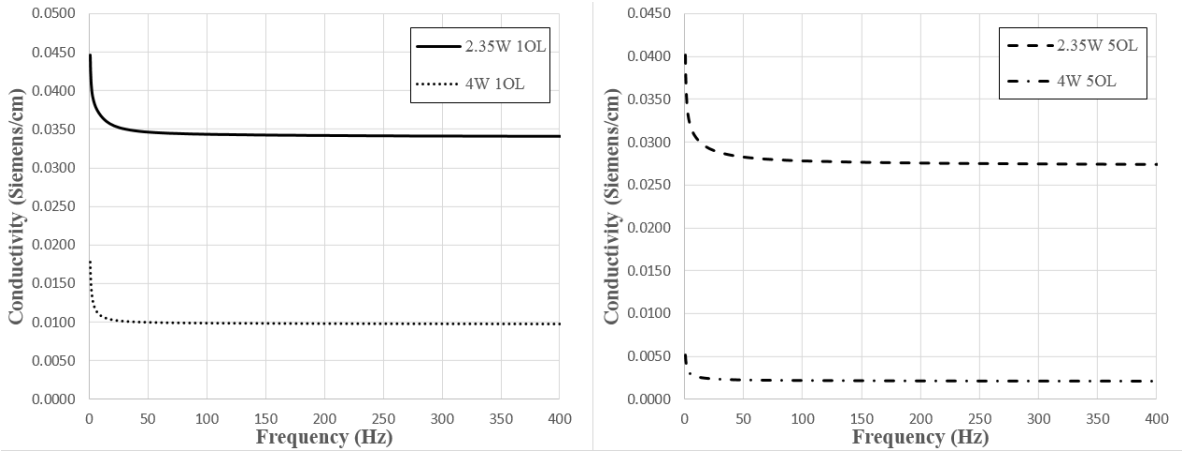

Fig. 43 Conductivity of thin film processed samples at 2.35 W and 4 W. (A) 1 OL, (B) 5 OL.

The effects of the overlaps were also compared as in Fig. 44. At both powers, the expected trend is seen where higher overlap numbers lead to higher surface temperatures and hence an increase in the evaporation of the thin film resulting in a decreased conductivity. However, at 4W the drop-in conductivity is much more significant. This can be related back to the increase in power where microparticle formation begins to occur.

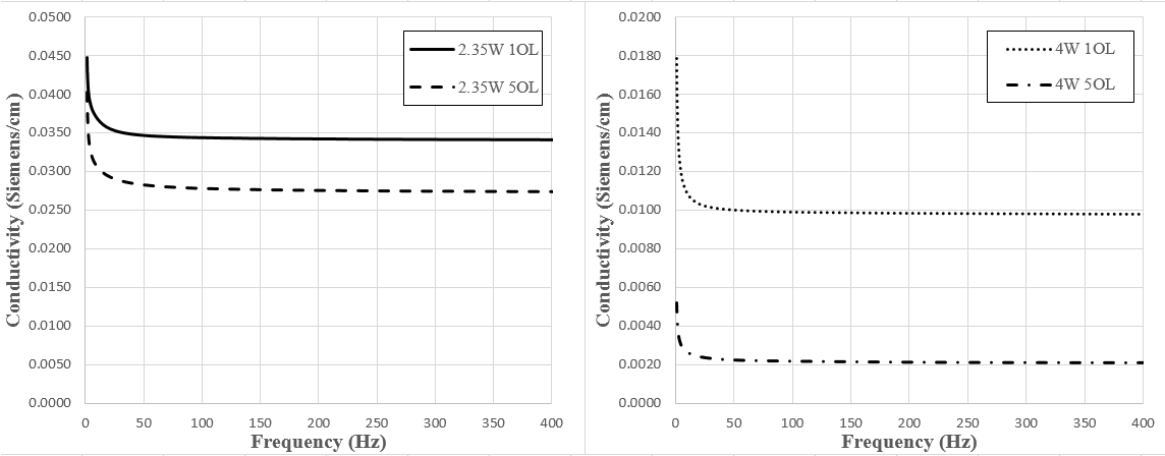

Fig. 44 Conductivity of thin film processed samples at 1 OL and 5 OL. (A) 2.35 W, (B) 4 W.

6.2 Biocompatibility

Untreated and laser treated thin film samples were analyzed through EDX. Both were immersed in a solution of SBF for a duration of five weeks. From Fig. 45, it is clear that the biocompatibility of the unprocessed thin film is lacking compared to the processed one. When compared to laser treated Silicon, higher levels of Chlorine, Sodium, Oxygen, and Phosphorous are found compared to the untreated samples. The increase in Calcium, Phosphorous, and Oxygen in the samples suggests the formation of bone-like apatite as these are important elements in its production in the body [27]. As mentioned in section 5.2, conclusive results cannot be made with the low sampling rate. A minimum of ten identical samples would need to be submerged in SBF to ensure accuracy of the results. Other testing methods should be employed in terms of cell culturing since SBF testing is only one of many available methods and acts only as a preliminary assessment. Cytotoxicity, although studied in previous researches with Gold and Silicon independently should be assessed as well. It is an effective, simple, and rapid evaluation technique to avoid toxicity prior to in-vivo testing. Cell growth, reproduction, and morphological should

also be evaluated [72]. Further in-vitro and in-vivo tests to be conducted should include different cell types such as tissue cells, fibroblasts, and osteoblasts.

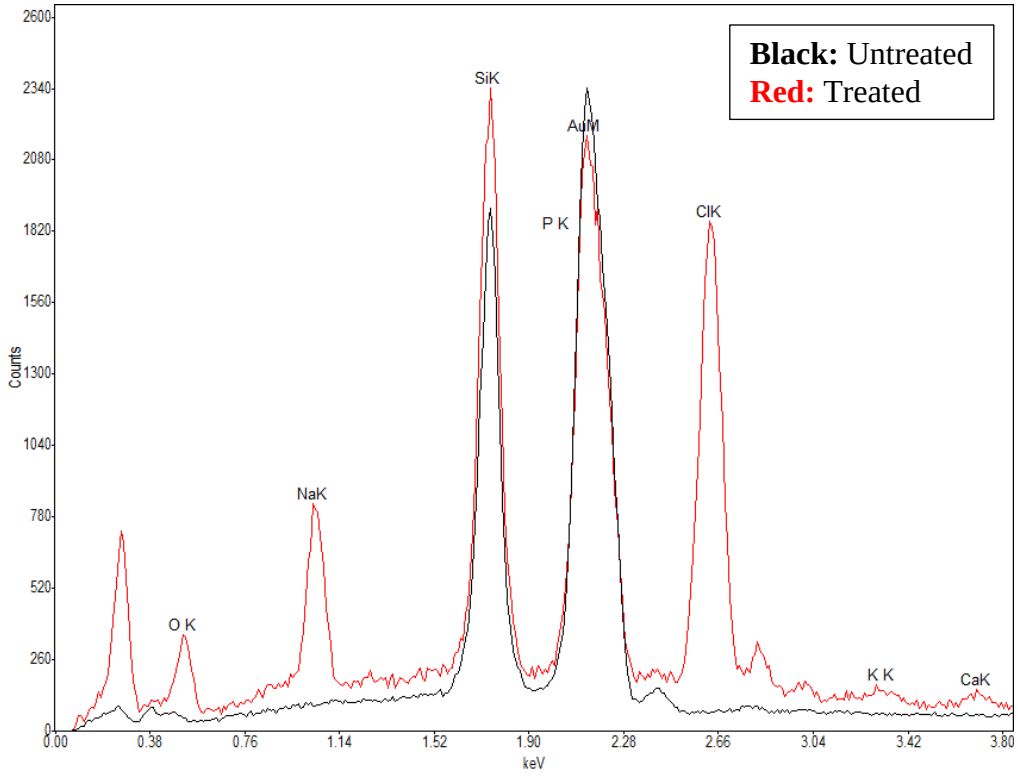

Fig. 45 EDX results of untreated and laser treated sample.

Chapter 7

7.0 Summary and Future Work

7.1 Summary

This thesis outlines an efficient and cost-effective method to both generate and customize the conductivity of porous and nanofibrous Silicon through the addition of Gold nanoparticles. This research will aid in the improvement of the viability of Silicon in biological sensing applications as well as in research pertaining to tissue engineering.

Micro and nanofibrous structures were achieved using a nanosecond Nd:YAG pulsed laser on both a single crystalline and an evaporated Gold Silicon wafer. The processed single crystalline Silicon samples were sputtered with Gold for either four or eight minutes to impart and analyze their conductive properties. The same was done with Silicon coated with a thin film of Gold. Power, overlap number, and line spacing were varied in this experiment and the changes in the absorption capabilities and electrical conductivity of the samples were measured and compared. The absorption was found to increase at smaller line spacings and at higher overlaps, allowing for the rearrangement of the Silicon substrate into fibers and agglomerates capable of absorbing more light. It was shown that both Gold and Silicon particles exhibited growth as the absorption coefficients of the materials increased. Fibrous structures were seen to form at shorter line spacings and at higher powers. As the overlap numbers were increased, the fiber diameters grew as well due to the growth in particle sizes. The conductivity was found to increase with increases in Gold

concentrations from the sputtering time. A decrease in the electrical conductivity of the samples could be related back to the Oxygen levels within the samples, where more Oxygen resulted in lower conductivity.

The thin film coated samples were processed at varying powers to decrease the evaporation of the Gold. The lower powers produced higher measurements of the overall Gold concentration of the samples. It was shown that both Gold and Silicon particles exhibited growth with increasing overlaps, but showed decreases in conductivities with the latter. The Gold interparticle distances were measured and showed the expected relationship with the conductivity of the samples. Shorter interparticle distances led to higher conductivities. As expected, thin film samples had much higher concentrations of Gold due to the comparatively thicker Gold coating compared to sputtered samples.

The overall biocompatibility of the samples was assessed with positive findings. It is suggested that both sputtered and Gold thin film samples that are laser treated have better biocompatibility properties than untreated samples. Although conclusive results couldn't be drawn, the formation of apatite on the surface was shown to be promoted through traces of Calcium, Oxygen, and Phosphorous on the surface. Further in-vitro and in-vivo studies are required in this area.

Although there is yet more research to be done in this area, these findings act as an important preliminary review as to the direction in which biosensing applications can be further adapted. Silicon, being a semiconductor and one of the most common resource for electronic and circuit building, can now impart conductive and biocompatible properties. This method outlines an economic, simple, and yet effective way to process Silicon to achieve nanoporous structures able to be both electrically conductive and allow for an

increased biocompatibility. Compared to other methods, this one involves less steps, is more cost-effective, and both processing time and wafer damage are reduced.

The main contributions of this research can be outlined as follows:

- Demonstrated the viability of generating porous and fibrous structures on the surface of single-crystalline and Gold coated Silicon using a nanosecond pulsed laser. The laser parameters were altered and the material and physical properties of the resulting structures were investigated and explained.
- Established the feasibility of imparting electrical conductive properties to the surface of laser processed Silicon as well as showing a level of controllability; the proposed techniques involve Gold sputtering processed Silicon and laser processing Gold coated Silicon which have both shown relationships between the laser parameters and the measured conductivities of the samples.
- Verified the preliminary biocompatibility of the processed Silicon using SBF; this method has shown and verified previous literary findings regarding the biocompatibility of Silicon dioxide. This research further shows the biocompatibility of Gold embedded within the Silicon dioxide.

7.2 Future Research

Future work in the application and enhancement of this research can be outlined as follows:

- Further investigative work regarding the conductivity of Silicon dioxide embedded with Gold using more precise tools such as a four-point-probe to obtain more quantitative data;
- Study other coating methods including but not limited to ALD and CVD methods;

- Consider different Silicon doped wafers including Gold doped;
- Investigate the effects of SBF on the conductivity of the samples;
- Further in-vitro testing should be conducted, where different cell types and their responses are investigated. It is also important to address the controllability of cell attachment using the outlined methods for the Silicon processing;
- With substantial in-vitro testing, the specimens should be tested in-vivo. With promising results, the development or coating of a biomedical sensor using this material should be attempted and tested.

8.0 References

[1] N. Huebsch and D. J. Mooney, "Inspiration and application in the evolution of biomaterials," *Nature,* vol. 462, no. 7272, pp. 426-432, 2009.

[2] S. Zhang, G. Wright, and Y. Yang, "Materials and techniques for electrochemical biosensor design and construction," *Biosensors and Bioelectronics,* vol. 15, no. 5, pp. 273-282, 2000.

[3] M. S. Brown and C. B. Arnold, "Fundamentals of laser-material interaction and application to multiscale surface modification," in *Laser precision microfabrication*: Springer, 2010, pp. 91-120.

[4] C. R. Schwartsmann, L. d. F. Spinelli, L. C. Boschin, A. K. Yépez, M. V. Crestani, and M. F. Silva, "Correlation between patient age at total hip replacement surgery and lifeexpectancy," *Acta ortopedica brasileira,* vol. 23, no. 6, pp. 323-325, 2015.

[5] M. Navarro, A. Michiardi, O. Castano, and J. Planell, "Biomaterials in orthopaedics," *Journal of the Royal Society Interface,* vol. 5, no. 27, pp. 1137-1158, 2008.

[6] D. Rickert, M. Moses, A. Lendlein, S. Kelch, and R. P. Franke, "The importance of angiogenesis in the interaction between polymeric biomaterials and surrounding tissue," *Clinical hemorheology and microcirculation,* vol. 28, no. 3, pp. 175-181, 2003.

[7] R. M. Pilliar, "Metallic biomaterials," in *Biomedical materials*: Springer, 2009, pp. 41-81.

[8] M. Saini, Y. Singh, P. Arora, V. Arora, and K. Jain, "Implant biomaterials: A comprehensive review," *World Journal of Clinical Cases: WJCC,* vol. 3, no. 1, p. 52, 2015.

[9] M. Kulkarni, A. Mazare, P. Schmuki, and A. Iglič, "Biomaterial surface modification of Titanium and Titanium alloys for medical applications," *Nanomedicine,* vol. 5, pp. 112-130, 2014.

[10] C. Elias, J. H. Lima, R. Valiev, and M. Meyers, "Biomedical applications of Titanium and its alloys," *JOM Journal of the Minerals, Metals and Materials Society,* vol. 60, no. 3, pp. 46-49, 2008.

[11] N. Huang *et al.,* "Hemocompatibility of Titanium oxide films," *Biomaterials,* vol. 24, no. 13, pp. 2177-2187, 2003.

[12] V. Challa, S. Mali, and R. Misra, "Reduced toxicity and superior cellular response of preosteoblasts to Ti-6Al-7Nb alloy and comparison with Ti-6Al-4V," *Journal of Biomedical Materials Research Part A,* vol. 101, no. 7, pp. 2083-2089, 2013.

[13] C. C. Gomes *et al.,* "Assessment of the genetic risks of a metallic alloy used in medical implants," *Genetics and molecular biology,* vol. 34, no. 1, pp. 116-121, 2011.

[14] P. Guo, "General Method for Producing Biodegradable Nanoparticles and Nanofibers Based on Nanoporous Membranes," University of Florida, 2011.

[15] M. Gajendiran *et al.,* "Conductive biomaterials for tissue engineering applications," *Journal of Industrial and Engineering Chemistry,* 2017.

[16] J. Shi and D. M. Porterfield, *Surface modification approaches for electrochemical biosensors*. INTECH Open Access Publisher, 2011.

[17] G. Shruthi, C. Amitha, and B. B. Mathew, "Biosensors: a modern day achievement," *Journal of Instrumentation Technology,* vol. 2, no. 1, pp. 26-39, 2014.
[18] K. Balasubramanian and M. Burghard, "Biosensors based on carbon nanotubes," *Analytical and bioanalytical chemistry,* vol. 385, no. 3, pp. 452-468, 2006.
[19] J. Davis, "Overview of biomaterials and their use in medical devices," *Handbook of materials for medical devices. Illustrated edition, Ohio: ASM International,* pp. 1-11, 2003.
[20] C.-M. Tîlmaciu and M. C. Morris, "Carbon nanotube biosensors," *Frontiers in chemistry,* vol. 3, 2015.
[21] N. Yang, X. Chen, T. Ren, P. Zhang, and D. Yang, "Carbon nanotube based biosensors," *Sensors and Actuators B: Chemical,* vol. 207, pp. 690-715, 2015.
[22] A. Eatemadi *et al.*, "Carbon nanotubes: properties, synthesis, purification, and medical applications," *Nanoscale Res Lett,* vol. 9, no. 1, p. 393, 2014.
[23] C. Jamois *et al.*, "New concepts of integrated photonic biosensors based on porous Silicon," *Biosensors-Emerging Materials and Applications,* 2011.
[24] C. Exley, "Silicon in life: a bioinorganic solution to bioorganic essentiality," *Journal of Inorganic Biochemistry,* vol. 69, no. 3, pp. 139-144, 1998.
[25] S. Dhanekar and S. Jain, "Porous Silicon biosensor: current status," *Biosensors and bioelectronics,* vol. 41, pp. 54-64, 2013.
[26] L. Buckberry and S. Bayliss, "Porous Silicon as a biomaterial," *Materials World,* vol. 7, no. 4, pp. 213-215, 1999.
[27] C. Colpitts, A. M. Ektesabi, R. A. Wyatt, B. D. Crawford, and A. Kiani, "JABFM," 2016.
[28] M. H. Jones and S. H. Jones, "Wet-chemical etching and cleaning of Silicon," *Fredericksburg, Va.: Virginia Semiconductor,* 2003.
[29] Z.-Y. Qiu, C. Chen, X.-M. Wang, and I.-S. Lee, "Advances in the surface modification techniques of bone-related implants for last 10 years," *Regenerative biomaterials,* vol. 1, no. 1, pp. 67-79, 2014.
[30] A. Kiani, K. Venkatakrishnan, and B. Tan, "Micro/nano scale amorphization of Silicon by femtosecond laser irradiation," *Optics express,* vol. 17, no. 19, pp. 16518-16526, 2009.
[31] S. K. Mitra and A. A. Saha, "Surface Modification, Methods," *Encyclopedia of Microfluidics and Nanofluidics,* pp. 3115-3123, 2015.
[32] M. Radmanesh and A. Kiani, "Bioactivity enhancement of Titanium induced by Nd: Yag laser pulses," *Journal of applied biomaterials & functional materials,* vol. 14, no. 1, 2016.
[33] J. Reif, "Basic physics of femtosecond laser ablation," in *Laser-Surface Interactions for New Materials Production*: Springer, 2010, pp. 19-41.
[34] A. Kiani, N. B. Patel, B. Tan, and K. Venkatakrishnan, "Leaf-like nanotips synthesized on femtosecond laser-irradiated dielectric material," *Journal of Applied Physics,* vol. 117, no. 7, p. 074306, 2015.
[35] B. Tan and K. Venkatakrishnan, "Synthesis of fibrous nanoparticle aggregates by femtosecond laser ablation in air," *Optics express,* vol. 17, no. 2, pp. 1064-1069, 2009.

[36] A. S. Mahmood, K. Venkatakrishnan, and B. Tan, "Gold-Silicon nanofiber synthesized by femtosecond laser radiation for enhanced light absorptance," *Nanoscale research letters,* vol. 9, no. 1, p. 255, 2014.
[37] M. Shaheen, J. Gagnon, and B. Fryer, "Femtosecond laser ablation behavior of Gold, crystalline Silicon, and fused silica: a comparative study," *Laser Physics,* vol. 24, no. 10, p. 106102, 2014.
[38] M. S. Gorji, A. R. Khairunisak, and K. Y. Cheong, "Deposition of Gold Nanoparticles on Linker-Free Silicon Substrate by Spin-Coating," in *Advanced Materials Research*, 2014, vol. 1024, pp. 124-127: Trans Tech Publ.
[39] R. Shukla, V. Bansal, M. Chaudhary, A. Basu, R. R. Bhonde, and M. Sastry, "Biocompatibility of Gold nanoparticles and their endocytotic fate inside the cellular compartment: a microscopic overview," *Langmuir,* vol. 21, no. 23, pp. 10644-10654, 2005.
[40] M. Gosau, M. Haupt, S. Thude, M. Strowitzki, B. Schminke, and R. Buergers, "Antimicrobial effect and biocompatibility of novel metallic nanocrystalline implant coatings," *Journal of Biomedical Materials Research Part B: Applied Biomaterials,* 2015.
[41] E. Hidalgo and C. Domınguez, "Study of cytotoxicity mechanisms of silver nitrate in human dermal fibroblasts," *Toxicology letters,* vol. 98, no. 3, pp. 169-179, 1998.
[42] M. B. Cortie, "The weird world of nanoscale Gold," *Gold Bulletin,* vol. 37, no. 1, pp. 12-19, 2004.
[43] G. Presnova *et al.*, "Biosensor based on a Silicon nanowire field-effect transistor functionalized by Gold nanoparticles for the highly sensitive determination of prostate specific antigen," *Biosensors and Bioelectronics,* vol. 88, pp. 283-289, 2017.
[44] H. Chang *et al.*, "Gold nanoparticles embedded Silicon channel biosensor for improved sensitivity," in *AIP Conference Proceedings*, 2016, vol. 1733, no. 1, p. 020074: AIP Publishing.
[45] W. Zhang, Y. Du, and M. L. Wang, "On-chip highly sensitive saliva glucose sensing using multilayer films composed of single-walled carbon nanotubes, Gold nanoparticles, and glucose oxidase," *Sensing and Bio-Sensing Research,* vol. 4, pp. 96-102, 2015.
[46] R. Mukherjee, "Correlation effects in nanoparticle composites: Percolation, packing and tunneling," 2014.
[47] V. Aroutiounian and M. Z. Ghulinyan, "Electrical conductivity mechanisms in porous Silicon," *physica status solidi (a),* vol. 197, no. 2, pp. 462-466, 2003.
[48] V. Lehmann, F. Hofmann, F. Möller, and U. Grüning, "Resistivity of porous Silicon: a surface effect," *Thin Solid Films,* vol. 255, no. 1-2, pp. 20-22, 1995.
[49] J.-H. Park and T. Sudarshan, *Chemical vapor deposition*. ASM international, 2001.
[50] D. M. Mattox, *Handbook of physical vapor deposition (PVD) processing*. William Andrew, 2010.
[51] F. Shimura, *Semiconductor Silicon crystal technology*. Elsevier, 2012.
[52] B. Averill and P. Eldredge, *General Chemistry: Principles, Patterns, and Applications*. The Saylor Foundation, 2011.

[53] C. Colpitis and A. Kiani, "Synthesis of bioactive three-dimensional Silicon-oxide nanofibrous structures on the Silicon substrate for bionic devices' fabrication," *Nanomaterials and Nanotechnology*, vol. 6, p. 8, 2016.
[54] M. J. Hancock, "18.303 Linear Partial Differential Equations, Fall 2004," 2004.
[55] L. Landau and E. Lifshitz, *Fluid mechanics: Landau and Lifshitz: course of theoretical physics*. Elsevier, 2013.
[56] E. G. Gamaly, A. V. Rode, and B. Luther-Davies, "Ultrafast ablation with high-pulse-rate lasers. Part I: Theoretical considerations," *Journal of Applied Physics*, vol. 85, no. 8, pp. 4213-4221, 1999.
[57] A. Kiani, K. Venkatakrishnan, and B. Tan, "Direct laser writing of amorphous Silicon on Si-substrate induced by high repetition femtosecond pulses," *Journal of Applied Physics*, vol. 108, no. 7, p. 074907, 2010.
[58] A. Tavangar, B. Tan, and K. Venkatakrishnan, "Study of the formation of 3-D titania nanofibrous structure by MHz femtosecond laser in ambient air," *Journal of Applied Physics*, vol. 113, no. 2, p. 023102, 2013.
[59] R. Fabbro, J. Fournier, P. Ballard, D. Devaux, and J. Virmont, "Physical study of laser-produced plasma in confined geometry," *Journal of applied physics*, vol. 68, no. 2, pp. 775-784, 1990.
[60] D. Devaux, R. Fabbro, L. Tollier, and E. Bartnicki, "Generation of shock waves by laser-induced plasma in confined geometry," *Journal of Applied Physics*, vol. 74, no. 4, pp. 2268-2273, 1993.
[61] E. K. Athanassiou, F. Krumeich, R. Grass, and W. J. Stark, "Advanced piezoresistance of extended metal-insulator core-shell nanoparticle assemblies," *Physical review letters*, vol. 101, no. 16, p. 166804, 2008.
[62] J. Srivastava, M. Prasad, and J. Wagner, "Electrical conductivity of Silicon dioxide thermally grown on Silicon," *Journal of The Electrochemical Society*, vol. 132, no. 4, pp. 955-963, 1985.
[63] I. Johansen, "Electrical conductivity in evaporated Silicon oxide films," *Journal of Applied Physics*, vol. 37, no. 2, pp. 499-507, 1966.
[64] B. Li, D. Yu, and S.-L. Zhang, "Raman spectral study of Silicon nanowires," *Physical Review B*, vol. 59, no. 3, p. 1645, 1999.
[65] T. Kokubo and H. Takadama, "How useful is SBF in predicting in vivo bone bioactivity?," *Biomaterials*, vol. 27, no. 15, pp. 2907-2915, 2006.
[66] A. Gaharwar, S. Sant, M. Hancock, and S. Hacking, *Nanomaterials in Tissue Engineering: Fabrication and Applications*. Elsevier, 2013.
[67] D. Sands, *Pulsed laser heating and melting*. INTECH Open Access Publisher, 2011.
[68] N. Singh, M. Razafinimanana, and A. Gleizes, "The effect of pressure on a plasma plume: temperature and electron density measurements," *Journal of Physics D: Applied Physics*, vol. 31, no. 20, p. 2921, 1998.
[69] C. Argile and G. Rhead, "Adsorbed layer and thin film growth modes monitored by Auger electron spectroscopy," *Surface Science Reports*, vol. 10, no. 6-7, pp. 277-356, 1989.
[70] P. Lewis, S. Micklethwaite, J. Harrington, M. Dixon, R. Brydson, and N. Hondow, "Exploring backscattered imaging in low voltage FE-SEM," in *Journal of Physics: Conference Series*, 2015, vol. 644, no. 1, p. 012019: IOP Publishing.

[71] O. Fesenko and L. Yatsenko, *Nanocomposites, Nanophotonics, Nanobiotechnology, and Applications: Selected Proceedings of the Second FP7 Conference and International Summer School Nanotechnology: From Fundamental Research to Innovations, August 25-September 1, 2013, Bukovel, Ukraine*. Springer, 2014.
[72] W. Li, J. Zhou, and Y. Xu, "Study of the in vitro cytotoxicity testing of medical devices (Review)," *Biomedical reports*, vol. 3, no. 5, pp. 617-620, 2015.
[73] A. Kiani, "Micro/Nano Amorphization/Oxidation Of Silicon Induced By High Repetition Femtosecond Laser Pulses," Doctor of Philosophy, Mechanical and Industrial Engineering, Ryerson University, Toronto, Ontario, 2013.
[74] C. Louis and O. Pluchery, *Gold nanoparticles for physics, chemistry and biology*. World Scientific, 2012.

Appendices

Appendix A

Properties of Silicon at Room Temperature

Table 2: Properties of Silicon at Room Temperature [73].

Structural and Mechanical	
Atomic Weight	28.09
Atoms, total (cm^{-3})	4.995×10^{22}
Crystalline Structure	Diamond (FCC)
Density (g/m^3)	2.33
Young's Modulus (GPa)	190
Poisson Ratio, v	0.27
Electrical	
Energy Gap (eV)	1.12
Intrinsic Carrier Concentration (cm^{-3})	1.38×10^{10}
Resistivity ($\Omega - cm$)	2.3×10^{5}
Thermal	
Thermal Expansion Coefficient ($℃^{-1}$)	2.6×10^{-6}
Melting Point (℃)	1414
Boiling Point (℃)	3265
Specific Heat (j/kgK)	700
Thermal Conductivity (W/mK)	150
Thermal Diffusivity (cm^2/s)	0.8

Properties of Gold at Room Temperature

Table 3: Properties of Gold at Room Temperature [74].

Structural and Mechanical	
Atomic Weight	196.97
Atoms, total (cm^{-3})	5.9×10^{22}
Crystalline Structure	FCC
Density (g/cm^3)	19.32
Young's Modulus (GPa)	79
Yield Strength (MPa)	205
Poisson Ratio, *v*	0.42
Electrical	
Energy Gap (eV)	1.84
Resistivity ($\Omega - cm$)	2.35×10^{-6}
Thermal	
Thermal Expansion Coefficient ($℃^{-1}$)	14×10^{-6}
Melting Point (℃)	1064
Boiling Point (℃)	2836
Specific Heat (j/kgK)	129
Thermal Conductivity (W/mK)	314
Thermal Diffusivity (m^2/s)	1.269

Appendix B

List of Publications

Refereed Journals

- Sarah Hamza, Anna Ignaszak, Amirkianoosh Kiani. “Synthesis of Au Nanoparticle-embedded Silicon Oxide Nanofibers by Laser Pulses and Sputtering Techniques for Biosensor Fabrication”, ***(Submitted; under review)
- Sarah Hamza, Amirkianoosh Kiani. “Silica/Gold Hybrid Nanofibers Induced by Laser Processing of Silicon Coated by Gold Thin-Film for Biomedical Sensing Applications” *** (Submitted; under review)

Refereed Conferences

- Sarah Hamza, Amirkianoosh Kiani. "Laser-Generated Silica Nanofibers Embedded with Electrospun Gold Nanoparticles: A Novel Platform for Biocompatible Sensing Devices" 33rd Annual Meeting of the Canadian Biomaterials Society (accepted)
- Sarah Hamza, Amirkianoosh Kiani. “A Rapid and Easy Procedure of Biosensor Fabrication by Nanosecond Laser Processing of Si Wafer Coated by Gold Thin-film” 5th International Conference on Bio-Sensing Technology (accepted)

Appendix C

ImageJ

Particle Measurements

1. Open the image to be analyzed within ImageJ
2. Zoom into the scale bar of the image
3. Draw a line across the bar (hold shift to keep the line straight)
4. Under “Analyze”, select “Set Scale”
5. In the known distance tab, type in the scale value of the image
6. In the “Unit of length” type the units of the image (ex. nm)
7. Click “OK”
8. Draw a line across the diameter of the particle to be measured
9. Press Ctrl and M at the same time to take the measurement
10. Repeat steps 8 and 9 for each particle needed to be measured
11. Once all the measurements are taken, right click in the measurements window and select “Summarize”
12. Right click again and select “Save As” to save the data to a file

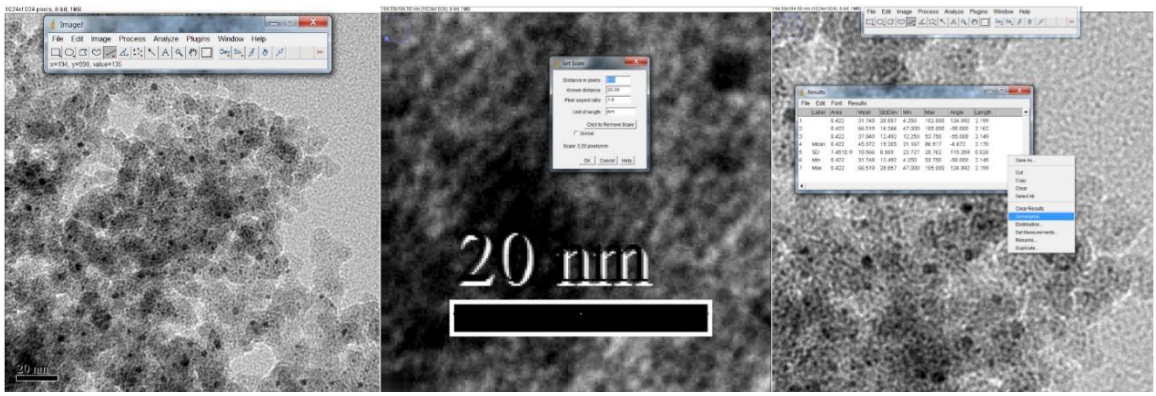

Concentration Measurements

1. Open the image to be analyzed within ImageJ (ensure that the image is cropped to only include the area needed to be analyzed)
2. Select “Image > Adjust > Brightness/Contrast”
3. Change the scales on the “B&C” window until only the particles you need to analyze show
4. Under “Analyze”, select “Histogram”
5. Click the “Live” button and select the area you would like to measure
6. The histogram will display a Mean and a Max value, which is the black to white ratio

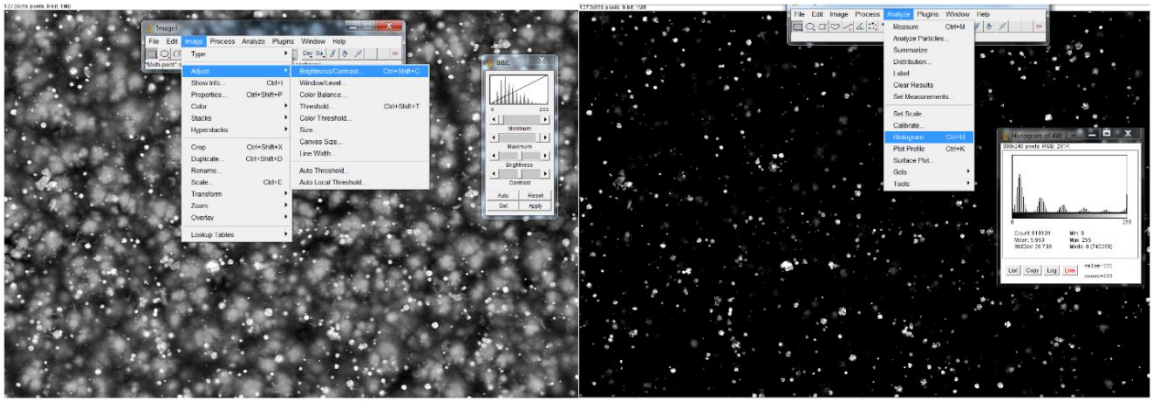

Curriculum Vitae

Name: Sarah Hamza

Education: University of New Brunswick
Bachelor of Science in Mechanical Engineering (2011-2015)

List of Publications

1. Refereed Journals

1. Sarah Hamza, Anna Ignaszak, Amirkianoosh Kiani. “Synthesis of Au Nanoparticle-embedded Silicon Oxide Nanofibers by Laser Pulses and Sputtering Techniques for Biosensor Fabrication”, ***(Submitted; under review)
2. Sarah Hamza, Amirkianoosh Kiani. “Silica/Gold Hybrid Nanofibers Induced by Laser Processing of Silicon Coated by Gold Thin-Film for Biomedical Sensing Applications” *** (Submitted; under review)

2. Refereed Conferences

1. Sarah Hamza, Amirkianoosh Kiani. "Laser-Generated Silica Nanofibers Embedded with Electrospun Gold Nanoparticles: A Novel Platform for Biocompatible Sensing Devices" 33rd Annual Meeting of the Canadian Biomaterials Society (accepted)
2. Sarah Hamza, Amirkianoosh Kiani. “A Rapid and Easy Procedure of Biosensor Fabrication by Nanosecond Laser Processing of Si Wafer Coated by Gold Thin-film” 5th International Conference on Bio-Sensing Technology (accepted)

3. Presentations

1. Sarah Hamza, A. Kiani (2016). “Conductivity of Laser Pulse Generated Nanofibrous Silicon Oxide Embedded with Gold”. Annual Mechanical Engineering Graduate Student Conference (MEGSC 2016). [Oral Presentation]